Heat Transfer and Combustion Simulation of Seven-Element O_2/CH_4 Rocket Combustor

Nikolaos Perakis,* Daniel Rahn,† and Oskar J. Haidn‡
Technical University of Munich, 85748 Garching, Germany
and
Daniel Eiringhaus§
ArianeGroup, GmbH, 82024 Taufkirchen, Germany

DOI: 10.2514/1.B37402

In the present Paper, the simulation of the flow inside an experimental GOX/GCH_4 rocket thrust chamber is undertaken. The combustor's injector consists of seven individual coaxial injector elements, while the chamber and nozzle segments are water cooled. The results presented in this Paper are obtained with three-dimensional Reynolds-averaged Navier–Stokes simulations using an adiabatic flamelet formulation for the chemistry modeling. The main focus is placed on examining the effect of the different turbulence models on the flame structure and on the resulting pressure and wall heat flux. The obtained numerical values are compared to experimental measurements, delivering good agreement in the heat flux profile at the combustion chamber wall and a slight underestimation of the pressure profile of approximately 2.5%. Greater discrepancies are observed in the heat flux of the nozzle segment but are largely attributed to the experimental setup. A conjugate heat transfer simulation of the structure and cooling channel flow confirms this assumption, and results for both one-way and two-way couplings are shown. It is demonstrated that a one-way coupling between hot gas and structure is sufficient due to the low sensitivity of the wall heat flux on the wall temperature. The azimuthal variation of the heat flux is also examined, and interestingly the heat flux showcases a local minimum at the position directly above the injector element. It is shown that an increased concentration of colder fuel-rich gas directly above the injector due to a strong vortex system leads to the local minimum in heat flux values and is strongly influenced by the injector/injector interaction near the face plate.

Nomenclature

c_p	=	specific heat capacity, J/(kg · K)
H	=	specific total enthalpy, J/kg
h	=	specific enthalpy, J/kg
k	=	turbulence kinetic energy, m^2/s^2
M	=	molar mass, kg/mol
$\dot{m}$	=	mass flow rate, kg/s
P	=	probability density function
Pr_t	=	turbulent Prandtl number
p	=	pressure, bar
$\dot{q}$	=	heat flux, W/m^2
R	=	universal gas constant, J/(mol · K)
r	=	grid refinement ratio
Sc_t	=	turbulent Schmidt number
T	=	temperature, K
t	=	time, s
U	=	unmixedness
u	=	velocity, m/s
x, y, z	=	spatial coordinates, m
Y	=	species mass fraction
y^+	=	dimensionless wall distance
Z	=	mixture fraction
Z'^2	=	mixture fraction variance
ϵ	=	turbulent dissipation, m^2/s^3
ε	=	numerical error
θ	=	angle, deg
λ	=	heat conductivity, W/(m · K)
μ	=	viscosity, Pa · s
ρ	=	density, kg/m^3
τ	=	stress tensor, N/m^2
ϕ	=	generic variable
χ	=	scalar dissipation rate, 1/s
ψ	=	apparent numerical order
ω	=	specific rate of dissipation, 1/s
Ω	=	vorticity, 1/s
$\dot{\omega}$	=	chemical reaction rate, 1/s

Subscripts

c	=	chamber
ext	=	exact
flow	=	flow
fu	=	fuel
k	=	species index
max	=	maximal value
N	=	nozzle
ox	=	oxidizer
sp	=	species
st	=	stoichiometric value
t	=	turbulent value

Presented as Paper 2018-4554 at the 2018 Joint Propulsion Conference, AIAA Propulsion and Energy Forum, Cincinnati, OH, 9–11 July 2018; received 2 October 2018; revision received 24 June 2019; accepted for publication 13 July 2019; published online 22 August 2019.

*Graduate Student, Chair of Turbomachinery and Flight Propulsion, Boltzmannstrasse 15; nikolaos.perakis@ltf.mw.tum.de.
†Graduate Student, Chair of Turbomachinery and Flight Propulsion.
‡Prof. Dr.-Ing., Chair of Turbomachinery and Flight Propulsion.
§Graduate Student, Robert-Koch-Strasse 1.

I. Introduction

A VERY important step in the process of designing and optimizing new components or subsystems for rocket propulsion devices is the numerical simulation of the flow and combustion in them. Implementing computational fluid dynamics (CFD) tools in the design process significantly reduces the development time and cost and allows for greater flexibility. The main requirements that a successful CFD tool must fulfill in order to be suitable for rocket engine applications is providing an accurate description of the heat loads on the chamber wall, the combustion pressure, the combustion efficiency, and the performance parameters such as the specific impulse [1]. Other design problems that can be

tackled with the use of CFD are prediction and simulation of combustion-acoustic instabilities [2].

The reliability of a numerical tool lies in accurately describing the physical and chemical processes taking place within the thrust chamber. This is done by a set of models (and the corresponding numerical methods to solve them), which must be validated for the wide range of operating conditions that can occur in different types of rocket engines (e.g., attitude control thrusters and launcher propulsion). To make CFD attractive in the design process, the choice of the used models should be such that the computational time does not become prohibitive, while still capturing the physics of the underlying phenomena with sufficient accuracy.

A significant step during the development of numerical tools for combustion and turbulence modeling in rocket engines is the validation of the models. Several studies have been carried out in an effort to describe the chemical and physical processes taking place in single-element rocket combustion chambers over the years. Oefelein and Yang [3] examined the flow and combustion in LOX/H_2 rocket engine configurations, whereas Zhukov [4] performed an analysis of a GOX/GH_2 single-element combustor. Cutrone et al. [5], on the other hand, performed Reynolds-averaged Navier–Stokes (RANS) simulations on single-element chambers operated with LOX/CH_4 using a real-gas flamelet/progress variable model, whereas Zips et al. [6] used a real-gas steady flamelet model for large-eddy simulation of a LOX/CH_4 combustor.

Compared to single-element chamber simulations, the available studies for multi-injector rocket thrust chambers are limited. Furthermore, most of the available multi-injector studies are devoted to LOX/hydrogen thrust chambers. Urbano et al. [2] examined the triggering of combustion instabilities in LOX/H_2 rocket engines, whereas Negishi et al. [7,8] carried out simulations of the combustion and wall heat transfer in multi-element oxygen/hydrogen rocket thrust chambers. In the case of hydrocarbon engines, a simplified approach for the prediction of wall heat transfer of methane combustion was proposed by Betti et al. [9] using a pseudoinjector RANS approach, which, however, tends to overestimate the heat flux in the near injection region and does not provide any information about the azimuthal heat load distribution. A similar approach using a uniform pseudoinjection with a nonadiabatic flamelet model was implemented by Kim et al. [10], who carried out simulations of multi-element rocket engines with hydrocarbons as fuel, without, however, performing an analysis of the wall heat transfer. Song and Sun [11], on the other hand, focused on the coupled wall heat transfer in multi-element methane rocket engines but did not provide a comparison of the simulations with experimental data.

Within the framework of facilitating the development of CFD for rocket engines, several different configurations of rocket combustors and propellant combinations have been tested as shown by Silvestri et al. [12], building an experimental database that can be used in the validation process of CFD models. In a similar manner as with the single-element GOX/GCH_4 rocket combustor described by Chemnitz et al. [13], a test case from the available experimental database is defined. The experimental rocket combustor is operated with gaseous oxygen (GOX) and gaseous methane (GCH_4) and has a multi-element injector. A detailed description of the test campaign can be found in the work by Silvestri et al. [14]. Section II gives a short summary of the relevant experimental data used in the simulations.

In the present Paper, the numerical results from the simulation of the seven-element chamber are presented. Having identified the absence of available numerical studies dealing with the combustion and wall heat transfer simulation of multi-element methane rocket combustors, the goal of this study is to examine the ability of existing turbulent combustion models to accurately predict performance and wall heat loads. A three-dimensional (3D) RANS approach is used, and the combustion modeling is based on the adiabatic flamelet approach. Compared to single-element combustors, multi-injector engines introduce additional physical phenomena needed to be described such as the interaction between individual jets and the wall flame impingement between neighboring elements. The objective of the study is not to introduce a new model but rather to evaluate the capability of existing ones to predict the mixing and interaction of the flames in multi-element methane/oxygen configurations.

To assess the strengths and weaknesses of the model, comparison with experimental data is necessary. Since the available measurements for the present test case only include calorimetric heat flux values for the coolant, a conjugate heat transfer simulation of structure and coolant is also applied. This step is, however, only considered in order to allow for a direct comparison with the measurements and to analyze the effect of the wall temperature on the wall heat transfer.

The present Paper is organized as follows. The experimental test case chosen for this analysis is described in Sec. II. Section III deals with the numerical setup and models applied in the hot gas simulation, whereas the results of the turbulent combustion are presented in Sec. IV. For the comparison with the experimental data, a one-way coupling as well as a fully conjugated heat transfer coupling with the structure and cooling channels is carried out, since the experimental calorimetric measurements do not coincide with the wall heat transfer as explained in Sec. V. The effect of the flame/flame interaction on the heat transfer characteristics is analyzed in Sec. VI. Finally, Sec. VII gives an overall conclusion and summary of the results and points out the potential areas of improvement.

II. Description of Test Case

The examined multi-injector combustion chamber was designed for GOX and GCH_4, allowing high chamber pressures (up to 100 bar) and film cooling behavior examination. One of the key aspects of the project is to improve the knowledge of heat transfer processes and cooling methods in the combustion chamber, which is mandatory for the engine design. The attention is focused, in particular, on injector/injector and injector/wall interaction. To have a first characterization of the injectors' behavior, the multi-element combustion chamber is tested at low combustion chamber pressures and for a wide range of mixture ratios [12].

The seven-element rocket combustion chamber has an inner diameter of 30 mm and a contraction ratio of 2.5 in order to achieve Mach numbers similar to the ones in most rocket engine applications. The combustion chamber, depicted in Fig. 1, consists of four cylindrical water-cooled chamber segments as well as a nozzle segment (individually cooled), adding up to a total length of 382 mm. For the current study, shear coaxial injector elements are integrated. The test configuration includes the GOX post being mounted flush with respect to the injection face. Table 1 gives an overview of the chamber and injector dimensions. Figure 2 shows the injector configuration as well as the locations of the cooling channels. The centers of the six outer injectors are located at a radial distance equal to 9 mm from the center of the central injector, which corresponds to 1.5 times the outer methane diameter D_{fu}, whereas their distance from the wall is equal to $D_{fu} = 6$ mm.

For the present test case, an operating point with mean combustion chamber pressure of 18.3 bar and mixture ratio of 2.65 is chosen. The experimental data made available for the numerical simulations include the mass flow rates of oxygen and methane, the wall temperature, the pressure profile, and integral heat flux values. A summary of the test data is given in Table 2. For the determination of

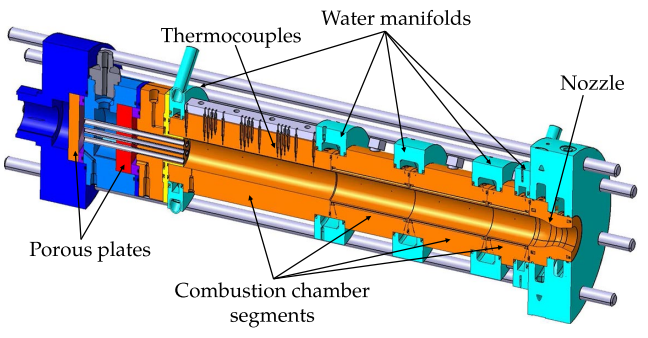

Fig. 1 Sketch of the combustion chamber.

Table 1 Summary of chamber dimensions

Dimension	Value, mm
Chamber diameter	30.0
Axial location end of segment A	145.0
Axial location end of segment B	222.0
Axial location end of segment C	299.0
Axial location end of segment D	340.0
Nozzle length	42.0
Total chamber length	382.0
Oxygen port diameter	4.0
Methane annulus inner diameter	5.0
Methane annulus outer diameter	6.0

Table 2 Summary of experimental data

Measured quantity	Value
Mean chamber pressure p_c, bar	18.3
Oxidizer to fuel ratio O/F	2.65
Oxidizer mass flow rate $\dot{m}_{\mathrm{ox}}$, kg/s	0.211
Fuel mass flow rate $\dot{m}_{\mathrm{fu}}$, kg/s	0.080
Average heat flux $\dot{q}_A$, MW/m^2	3.40
Average heat flux $\dot{q}_B$, MW/m^2	6.47
Average heat flux $\dot{q}_C$, MW/m^2	6.72
Average heat flux $\dot{q}_D$, MW/m^2	5.37
Average heat flux $\dot{q}_N$, MW/m^2	13.18

the heat flux values in the four chamber segments (A–D) and the nozzle (N), a calorimetric method is applied. The average heat flux of each chamber segment is determined by the enthalpy difference of the coolant between the inlet and outlet. This is obtained by precise temperature measurements in the water manifolds between the test segments. Two separate cooling cycles are implemented: one for the first four segments in the combustion chamber and an additional cooling cycle for the nozzle segment. The cross sections of the cooling channels in segments A–D are shown in Fig. 2 and further elaborated in Sec. IV. The temperature values available are obtained at radial distances of 0.7–1.0 mm from the hot gas wall and are used as boundary conditions for the calculation, as will be elaborated on in Sec. III.

III. Computational Setup of Hot Gas Simulation

The numerical simulation of the turbulent combustion within the seven-element chamber is carried out using the pressure-based code ANSYS Fluent, in which the 3D RANS equations are solved with the SIMPLE algorithm.

A. Computational Domain

The computational domain considered in the RANS calculation of the turbulent combustion consists of a 30 deg segment of the thrust chamber, which includes only a half-injector in the outer row and corresponds to 1/12th of the whole chamber. To create a developed velocity profile at the injection plane, the injector tubes are also modeled as can be seen in Fig. 3. The final mesh consists of approximately 2.9 million cells and is chosen after a mesh convergence study. To resolve the boundary layer appropriately and to facilitate a correct heat load prediction, the mesh in the vicinity of walls is refined to satisfy the condition $y^+ \approx 1$. A close-up view of the mesh at the injector and face plate is shown in Fig. 4. The black cells represent the posttip between oxygen and fuel, and the red and blue cells represent the CH_4 and O_2 inlets respectively. As can be seen in the right subfigure of Fig. 4, the x axis represents the axial direction, a notation that will be used throughout the entirety of the Paper. The origin of the x axis is located at the axial location of the face plate, i.e., at the location where the injector elements end and the chamber begins.

The grid is chosen after an extensive grid convergence study. To assess the influence of grid resolution, the maximal pressure and maximal heat flux on the thrust chamber wall are chosen as characteristic quantities, and the simulation is carried out using the standard $k-\epsilon$ model for the turbulence closure. Four meshes are evaluated, with the coarsest one consisting of approximately 1.8 million cells and the finest one consisting of 6.2 million cells.

To evaluate the convergence of the solution, the theory of the Richardson extrapolation [15] is employed. The numerical error is calculated by comparing the solutions on each grid to a value gained from Richardson extrapolation according to

$$\phi_{\mathrm{ext}} = \frac{r^{\psi} \cdot \phi_1 - \phi_2}{r^{\psi} - 1} \tag{1}$$

where the lower indices represent the finer mesh solutions, r is the grid refinement ratio, and ψ is the achieved numerical order.

The results are summarized in Table 3, whereas Fig. 5 shows the numerical error as a function of the grid points. Although only the results for the maximal pressure and heat flux values are shown, the analysis has been carried out for a larger set of representative points along the chamber wall, all of which demonstrate a similar behavior. All simulations are carried out with a second-order upwind scheme for all transport equations. The achieved order ψ of convergence is also estimated for each of the three variables, using the method shown in Eq. (2):

$$\psi = \frac{\log((\phi_3 - \phi_2)/(\phi_2 - \phi_1))}{\log r} \tag{2}$$

For all monitored variables, apparent orders between 1.75 and 1.90 are obtained.

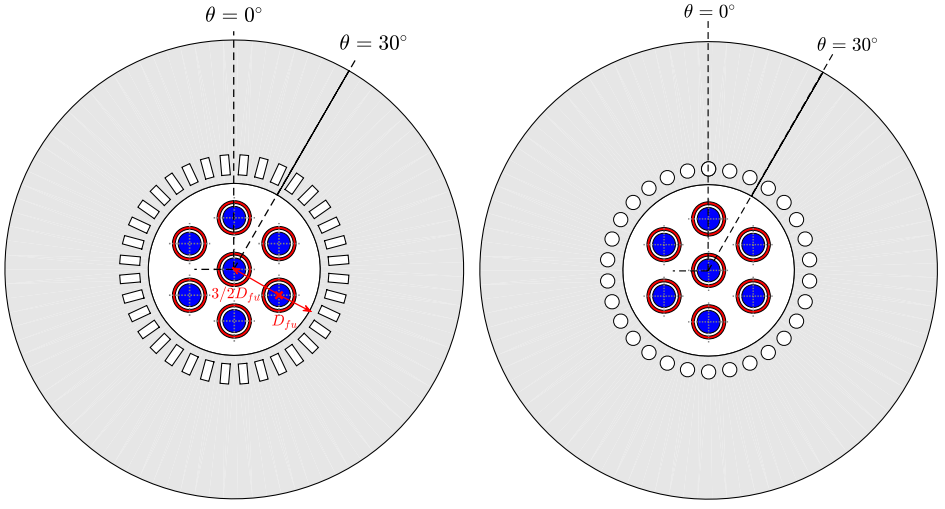

Fig. 2 View of the injector configuration and cross-section of the chamber in segment A (left) and in segments B, C, and D (right).

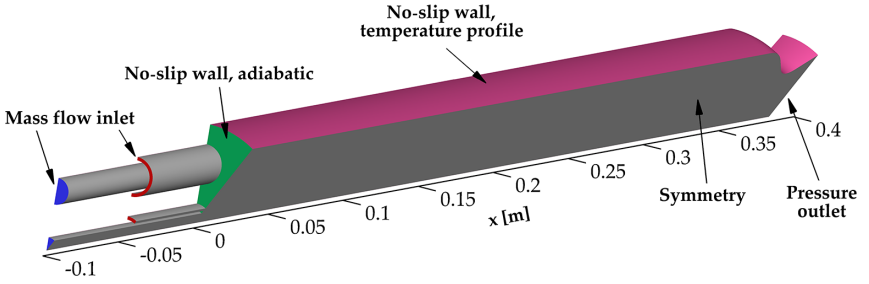

Fig. 3 Computational domain and applied boundary conditions.

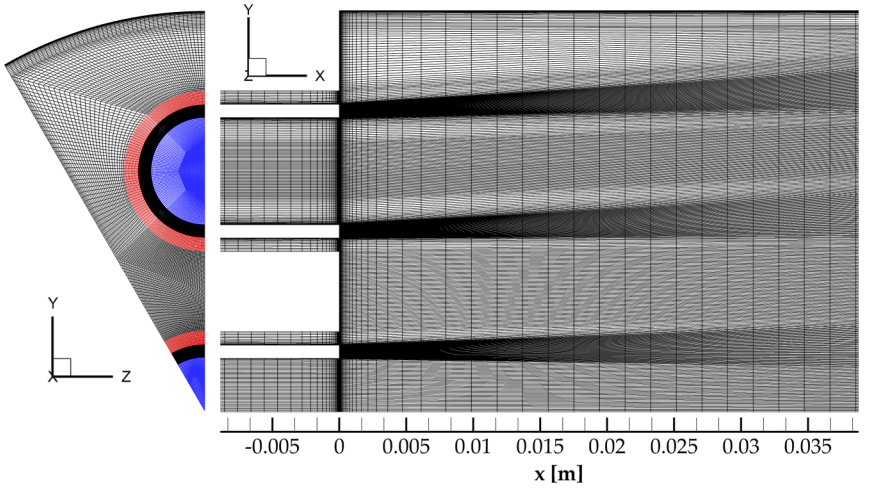

Fig. 4 Mesh at injector elements, face plate, and symmetry plane.

The relative numerical errors for the chosen grid ("Middle 1") remain underneath 2%, and for that reason, all simulations presented in this Paper are performed with it.

B. Boundary Conditions

A schematic representation of the applied boundary conditions can be seen in Fig. 3. The oxygen and methane inlets of the coaxial injector are defined as mass flow inlets by prescribing the appropriate values from the experiments. For the outlet, a pressure boundary condition is applied. The planes corresponding to 0 and 30 deg are defined as symmetry boundary conditions. This is chosen to reduce the computational time of the simulation and to take advantage of the RANS formulation, which gives only the mean flow values. A further justification of this choice for the boundary condition is given in Sec. VI. At the chamber wall, a prescribed temperature profile is defined. This profile is obtained by the experimental values. Since the temperature measurements directly at the hot gas wall are not available, the ones measured by the thermocouples located at radial distances of 0.7 and 1.0 mm from the hot gas wall are chosen instead. Since no temperature data are known at the nozzle, the last temperature value from the combustion chamber is defined at the nozzle wall. The resulting temperature profile at the wall is shown in Fig. 6. The validity of this boundary condition is assessed in Sec. V. All remaining walls are defined as adiabatic thermal boundaries and are given a no-slip condition.

Table 3 Results of the grid convergence study

Quantity	Coarse	Middle 1	Middle 2	Fine	Exact
Cells	$1.80 \cdot 10^6$	$2.91 \cdot 10^6$	$4.35 \cdot 10^6$	$6.1 \cdot 10^6$	— —
$p_{\max}$, bar	18.31	18.44	18.50	18.53	18.55
$\epsilon_{p_{\max}}$, %	1.27	0.57	0.25	0.09	— —
$\dot{q}_{\max}$, MW/m^2	17.42	16.95	16.78	16.70	16.69
$\epsilon_{\dot{q}_{\max}}$, %	4.37	1.55	0.53	0.11	— —

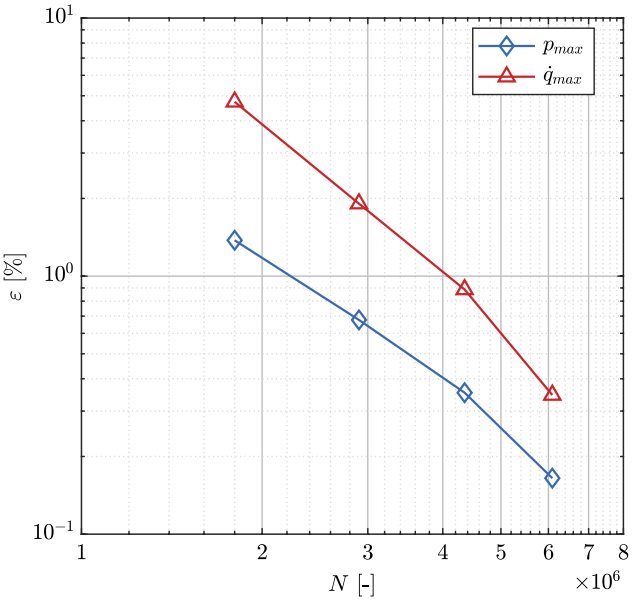

Fig. 5 Numerical error as a function of node number.

C. Numerical Models

The flowfield in the combustion chamber is described by the conservation equations for mass, momentum, and energy in three-dimensional space,

$$\frac{\partial \rho}{\partial t} + \frac{\partial (\rho \tilde{u}_i)}{\partial x_i} = 0 \tag{3}$$

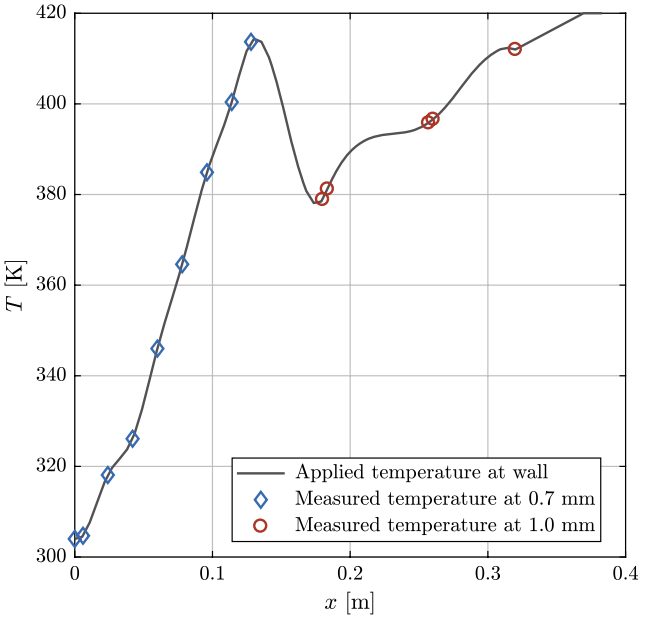

Fig. 6 Temperature at thrust chamber wall.

$$\frac{\partial(\bar{\rho}\tilde{u}_i)}{\partial t}+\frac{\partial(\bar{\rho}\tilde{u}_i\tilde{u}_j)}{\partial x_j}=-\frac{\partial\bar{p}}{\partial x_i}+\frac{\partial}{\partial x_i}(\bar{\tau}_{ij}-\bar{\rho}\,\widetilde{u_i''u_j''}) \tag{4}$$

$$\frac{\partial(\bar{\rho}\,\tilde{H})}{\partial t}+\frac{\partial(\bar{\rho}\,\tilde{H}\,\tilde{u}_i)}{\partial x_i}=\frac{\partial}{\partial x_i}\left(\frac{\bar{\lambda}}{\bar{c}_p}\frac{\partial\tilde{H}}{\partial x_i}-\bar{\rho}\,\widetilde{u_i''H''}\right) \tag{5}$$

where ρ and p are the Reynolds-averaged density and pressure, respectively, and $\tilde{u}_i$ are the Favre-averaged velocity components in the spatial directions x_i. The viscous stress tensor τ_{ij} is given as

$$\bar{\tau}_{ij}=\mu\left(\frac{\partial\tilde{u}_i}{\partial x_j}+\frac{\partial\tilde{u}_j}{\partial x_i}-\frac{2}{3}\delta_{ij}\frac{\partial\tilde{u}_k}{\partial x_k}\right) \tag{6}$$

with μ being the dynamic viscosity. The total specific enthalpy is $\tilde{H}$ and is defined as the sum of the static specific enthalpy $\tilde{h}$ and the specific kinetic energy $1/2\tilde{u}_i\tilde{u}_i$, while c_p and λ are the specific heat capacity and the thermal conductivity of the fluid. NASA polynomials are implemented for the enthalpy and heat capacity of the individual species. The mixture values are obtained using a mass fraction averaging:

$$\tilde{h}=\sum_{k=1}^{N_{sp}}\tilde{Y}_k\cdot\tilde{h}_k \tag{7}$$

$$\bar{c}_p=\sum_{k=1}^{N_{sp}}\tilde{Y}_k\cdot\bar{c}_{p,k} \tag{8}$$

A pressure-based scheme is used for the solution of the discretized equations. Density and pressure are coupled through the ideal gas equation of state,

$$\rho=\frac{pM}{R\tilde{T}} \tag{9}$$

where R is the universal gas constant and $\tilde{T}$ and M are the fluid mixture temperature and molecular weight, respectively.

1. *Turbulence Modeling*

The turbulent closure of the unclosed terms introduced by the Reynolds averaging of the Navier–Stokes equations is achieved by employing the Boussinesq hypothesis, relating the Reynolds stresses to the mean velocity gradients. Hence, the momentum stresses in Eq. (4) are modeled as

$$\bar{\rho}\,\widetilde{u_i''u_j''}=-\mu_t\left(\frac{\partial\tilde{u}_i}{\partial x_j}+\frac{\partial\tilde{u}_j}{\partial x_i}-\frac{2}{3}\delta_{ij}\frac{\partial\tilde{u}_k}{\partial x_k}\right)+\frac{2}{3}\bar{\rho}\,\tilde{k} \tag{10}$$

In this formulation, μ_t is the turbulent viscosity, and k is the turbulent kinetic energy.

Similarly, the closure of the turbulent heat flux in Eq. (5) is achieved using the turbulent Prandtl number Pr_t:

$$\bar{\rho}\,\widetilde{u_i''H''}=-\frac{\lambda_t}{\bar{c}_p}\frac{\partial\tilde{H}}{\partial x_i}=-\frac{\mu_t}{Pr_t}\frac{\partial\tilde{H}}{\partial x_i} \tag{11}$$

Rather than being a fixed species property, the value of the turbulent Prandtl number depends on the studied case. The evaluation of this quantity from an experimental point of view is found in the work by Kays [16], whereas Riedmann et al. [17] have analyzed the relevance of this number in the context of rocket combustor simulations. A constant value equal to 0.9 was chosen for the present study.

To evaluate the fluxes as defined previously, the turbulent viscosity needs to be modeled. In this Paper, two-equation models are considered, within which the turbulent viscosity is calculated from a turbulent length and time scale.

Specifically, in the standard k-ϵ model proposed by Launder and Spalding [18], one transport equation is solved for the turbulence kinetic energy $\tilde{k}=1/2\cdot\widetilde{u_i''u_i''}$, and one is solved for its dissipation $\tilde{\epsilon}$. To account for the proper treatment of the wall when using the $k-\epsilon$ model, the two-layer approach by Wolfshtein [19] is implemented.

In the $k-\omega$ shear-stress transport (SST) model by Menter et al. [20], on the other hand, two additional transport equations for the turbulent kinetic energy $\tilde{k}$ and the specific dissipation rate $\tilde{\omega}$ are solved instead.

The turbulent viscosity for the two models is then found by the relation

$$\mu_t\sim\bar{\rho}\frac{\tilde{k}^2}{\tilde{\epsilon}}\quad\text{and}\quad\mu_t\sim\bar{\rho}\frac{\tilde{k}}{\tilde{\omega}} \tag{12}$$

All modeling constants and blending functions are set to the proposed standard values by Launder and Spalding [18], Menter [20], and Wilcox [21].

2. *Chemistry Modeling*

As already mentioned, the chemistry modeling takes place by using the flamelet approach. This model significantly reduces the computational resources required for combustion simulations by reducing the number of transport equations. This is done by replacing the transport equations for the chemical species by only two equations: one for the mean mixture fraction $\tilde{Z}$ and one for its variance $\tilde{Z}''^2$, which is included in order to account for the interaction between the chemistry and the turbulence,

$$\frac{\partial(\bar{\rho}\,\tilde{Z})}{\partial t}+\frac{\partial(\bar{\rho}\tilde{u}_i\tilde{Z})}{\partial x_i}=\frac{\partial}{\partial x_i}\left(\frac{\mu+\mu_t}{Sc_t}\frac{\partial\tilde{Z}}{\partial x_i}\right) \tag{13}$$

$$\frac{\partial(\bar{\rho}\,\widetilde{Z''^2})}{\partial t}+\frac{\partial(\bar{\rho}\tilde{u}_i\widetilde{Z''^2})}{\partial x_i}=\frac{\partial}{\partial x_i}\left(\frac{\mu+\mu_t}{Sc_t}\frac{\partial\widetilde{Z''^2}}{\partial x_i}\right)+C_g\mu_t\frac{\partial\tilde{Z}}{\partial x_i}\frac{\partial\tilde{Z}}{\partial x_i}-C_d\bar{\rho}\frac{\tilde{\epsilon}}{\tilde{k}}\widetilde{Z''^2} \tag{14}$$

Here, Sc_t is the turbulent Schmidt number, which is set to a constant value of $Sc_t=0.6$ throughout the domain, and C_g and C_d are constants with values of 2.86 and 2.0, respectively [22].

A third variable, which is calculated by the model (but with an algebraic equation instead of a transport one), is the scalar dissipation rate $\tilde{\chi}$. This represents the dissipative term in the equation for the mixture fraction variance and is a measure for the deviation of the flow from equilibrium. A value of $\tilde{\chi}$ equal to zero would imply a perfect mixing and a low strain rate in the flow and would correspond to chemical equilibrium. For much higher values of this quantity, the extinction limit of the flame is reached [23],

$$\tilde{\chi} = \frac{C_\chi \tilde{\epsilon} \widetilde{Z''^2}}{\tilde{k}} \tag{15}$$

where C_χ is a constant with a value of 2.0.

The properties of the mixture such as the mixture fractions of the individual species as well as the temperature are pretabulated as a function of the laminar variables Z and χ_{st}. This is done by solving the flamelet equations in a preprocessing step. They consist of a transport equation for the temperature T and for the species mass fractions Y_i as shown in Eqs. (16) and (17) [24]:

$$\rho \frac{\partial T}{\partial t} = \frac{1}{2}\rho\chi \frac{\partial^2 T}{\partial Z^2} - \frac{1}{c_p}\sum_k^{N_{sp}} h_k \dot{\omega}_k + \frac{1}{2c_p}\rho\chi\left[\frac{\partial c_p}{\partial Z} + \sum_k^{N_{sp}} c_{p,k}\frac{\partial Y_k}{\partial Z}\right]\frac{\partial T}{\partial Z} \tag{16}$$

$$\rho \frac{\partial Y_k}{\partial t} = \frac{1}{2}\rho\chi \frac{\partial^2 Y_k}{\partial Z^2} + \dot{\omega}_k \tag{17}$$

In this context, $\dot{\omega}_k$ represents the species reaction rate, and h_k is the specific enthalpy of each species. The scalar dissipation rate is modeled using the one-parametric distribution [23]:

$$\chi(Z) = \chi_{st} \cdot \exp[2(erfc^{-1}(2Z_{st}))^2 - 2(erfc^{-1}(2Z))^2] \tag{18}$$

The flamelet equations are solved for different values of the scalar dissipation, and pressure leading to a laminar table $T, Y_k, \phi = f(Z, \chi_{st}, p)$, with ϕ representing the rest of the thermochemical variables such as density, specific heat capacity, and transport properties. To account for the turbulence/chemistry interaction, a further step is undertaken during preprocessing. A statistical treatment of turbulence is included by performing an integration using a presumed probability density function (PPDF). The resulting mean species mass fractions and mean temperature are hence tabulated as a function of the flow variables $\tilde{Z}, \widetilde{Z''^2}, \tilde{\chi}_{st}, \tilde{p}$. The PPDF chosen in this work is a decoupled probability density function (PDF), i.e., $P(Z, \chi_{st}, p) = P(Z) \cdot P(\chi_{st}) \cdot P(p)$, with a beta PDF for the mixture fraction and a Dirac function for the scalar dissipation and pressure.

During the CFD computation, the transport equations for the mean mixture fraction and its variance are solved, while the scalar dissipation is computed algebraically for each cell. The pressure is available from the pressure-based solver (using the SIMPLE algorithm). With this information, the species mass fractions are interpolated from the precomputed flamelet table. With the specific enthalpy of the cell, the temperature can be obtained. In the present Paper, an adiabatic (or else frozen) flamelet approach is used. This means that the mass fractions are not tabulated as a function of the enthalpy. This simplification suppresses further reactions, which could take place in the presence of a lower enthalpy, for example, recombinations close to the wall. Although this effect is considered to be significant and is probably not negligible, in the present Paper, the model has been simplified, and the enthalpy is only used to correct the resulting temperature (and hence density as well). One the other hand, the pressure dependence in the table accounts for the change in density during expansion in the rocket engine nozzle.

Various methods have been introduced in an effort to account for the additional reactions in the presence of the low-enthalpy environment, which is introduced in the vicinity of cooled walls. Methods using additional source terms in the flamelet equations [25–27], conductive heat losses [28,29], radiative losses [30,31], reductions of the chemical source term [32,33], permeable thermal walls [34], and enthalpy prescription methods [27] have been developed. Despite the simplification introduced, the adiabatic flamelet model is still widely used in the design process of rocket thrust chambers. For that reason, the present Paper aims at assessing its performance in dealing with multi-injector rocket combustor configurations.

The reaction mechanism used for the solution of the flamelets is the one by Slavinskaya et al. [35] and consists of 21 species and 97 reactions, whereas the thermodynamic properties were calculated using NASA polynomials. For the molecular transport (viscosity and thermal conductivity), the Chapman–Enskog kinetic theory [36,37] is used for the individual species, combined with the Wilke mixture rule [38], leading to species- and temperature-dependent properties. Different turbulence models are compared as seen in Sec. IV, but the standard $k-\epsilon$ model [18] shows the most promising results, using a two-layer model for the wall treatment [19].

IV. Results of Hot Gas Simulation

In this section, the results of the CFD calculations will be presented and compared with the experimental values. In the first approach, the standard $k-\epsilon$ [18], combined with the two-layer model [19] at the wall, is implemented and compared to the $k-\omega$ SST [20]. For both approaches, the closure of the turbulent flux terms is done with a turbulent Schmidt number $Sc_t = 0.6$ and a turbulent Prandtl number $Pr_t = 0.9$.

In Fig. 7, the temperature field inside the thrust chamber is plotted. Although a 30 deg domain is simulated, a larger domain (150 deg) is shown in the plots for a more intuitive visual representation. In the same plot, the line corresponding to stoichiometric composition ($Z_{st} = 0.2$) in the case of CH_4/O_2 combustion is indicated. This is included to give insight into the shape of the flame and consequently its length.

A. Effect of Turbulence Model on Mixing and Combustion

By examining the two distributions, it is evident that the $k-\epsilon$ models tends to better capture the mixing within the combustion chamber. Using the SST model, the temperature stratification remains prominent even in axial positions close to the nozzle. The temperature demonstrates namely a wavy pattern especially close to the wall, which is an indication for inefficient mixing of the individual flames. In the $k-\epsilon$, however, this temperature stratification is restricted to the first two-thirds of the engine, and a more homogeneous field is present farther downstream. The effect of the less efficient mixing is also evident by the length of the individual flames. In the $k-\epsilon$ solution, the outer and inner flames are almost equally long and extend up until the middle of the chamber. The SST, on the other hand, produces a sufficiently longer flame length, more dominantly in the outer flame implying a smaller flame/flame and flame/wall interaction.

The effect is attributed to a lower production in the turbulent viscosity of the SST model. Figure 8 demonstrates that the turbulent viscosity resulting from the $k-\epsilon$ calculation has a higher value throughout the whole combustion chamber, leading to a higher dissipation and hence a more uniform temperature field. The effect is mainly prominent in the area of the individual flame jets and in the core flow. The $k-\epsilon$ calculation is performed with the use of a limiter for the turbulent kinetic energy according to Menter [20]. Calculations without the limiter resulted in the presence of a large area with very high turbulent viscosity at the nozzle. This effect was restrained close to the axis of the nozzle and was dampened out closer to the wall. Although the production limiter led to the disappearance of this hot spot, making the μ_t field more intuitive, no measurable changes in the macroscopic values such as pressure or heat flux in the nozzle were observed.

A more quantitative examination of the inefficient mixing in the chamber is given by evaluating the unmixedness and the average O_2 mass fraction in the thrust chamber. The unmixedness is a dimensionless number that describes the degree of mixing in the chamber. For an ideal mixture, it reaches the value 0, whereas for

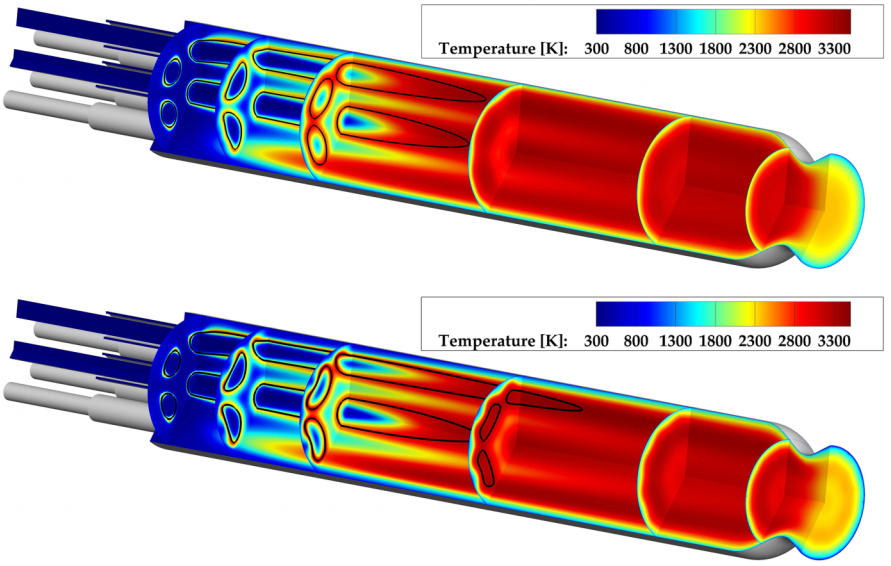

Fig. 7 Temperature field in the thrust chamber using the standard $k-\epsilon$ model (top) and the $k-\omega$ SST model (bottom). The black line corresponds to the stoichiometric mixture fraction. Axial scaling 50%.

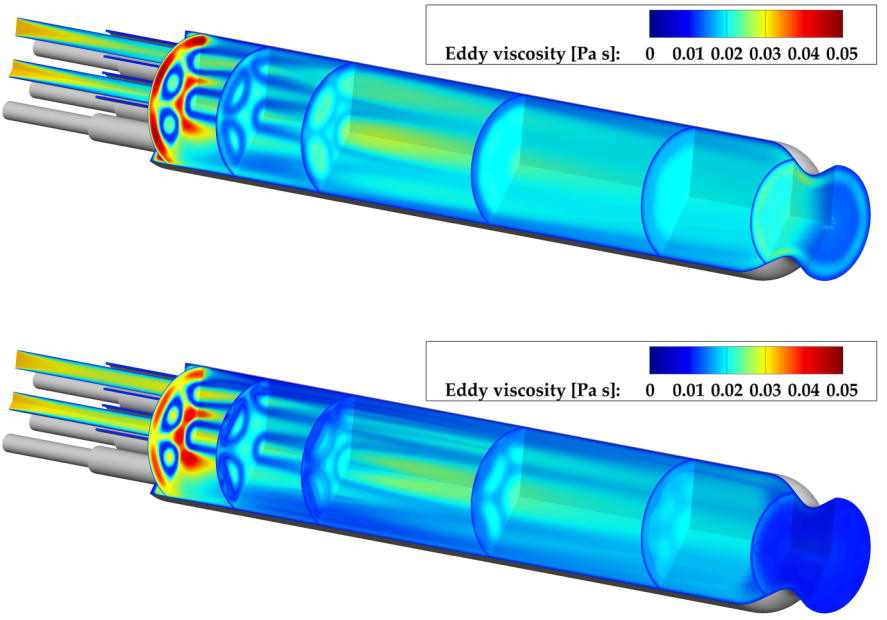

Fig. 8 Turbulent viscosity field in the thrust chamber using the standard $k-\epsilon$ model (top) and the $k-\omega$ SST model (bottom). Axial scaling 50%.

totally unmixed compounds, it is equal to 1. Its formula is given by Eq. (19):

$$U = \frac{\langle Z''^2 \rangle}{\langle Z \rangle (1 - \langle Z \rangle)} \tag{19}$$

$\langle Z \rangle$ stands for the average mixture fraction along all the nodes of a cross-sectional plane, and $\langle Z''^2 \rangle$ stands for the variance of the mixture fraction values on these points. The unmixedness should approach zero toward the exit plane of the nozzle, due to increasingly better mixing of the gas. In Fig. 9, the $k-\epsilon$ shows an unmixedness value approximately five times smaller at the exhaust plane and a generally lower value along the whole domain of the chamber, which confirms the fact that the mixing is calculated more effectively.

The fields of the heat release rate in Fig. 10 confirm these findings. We would like to point out that in the steady flamelet model the heat release rate is not a variable required by the solver, since the temperature is directly interpolated from the table for a given enthalpy, pressure, mixture fraction, variance, and scalar dissipation. However, similar to the thermochemical variables from the solution of the flamelet equations such as species mass fractions and temperature, it can be tabulated in the preprocessing state. The fields at the two symmetry planes as well as the $x = 0.2$ m plane are shown. As expected, the main heat release takes place within the shear layer, where the scalar dissipation rate is the highest. The energy release continues along the stoichiometric lines farther downstream and drops below 1% of the maximal value before the end of the chamber. In the case of SST, it can be observed that the heat release zones are much thinner and less diffuse than for the simulation with the $k-\epsilon$ model. This results in the energy being released for positions farther downstream, indicating that the mixing is not as efficient and that the combustion requires a longer length to be complete. This result is also in accordance with the heat flux values from Fig. 11.

A further quantity that acts as a measure for the degree of mixing and the completion of combustion is the concentration of oxygen in the combustion chamber. To achieve the maximum yield from the reaction of the propellants and hence the highest possible energy release, the amount of unburnt oxygen leaving the chamber should be

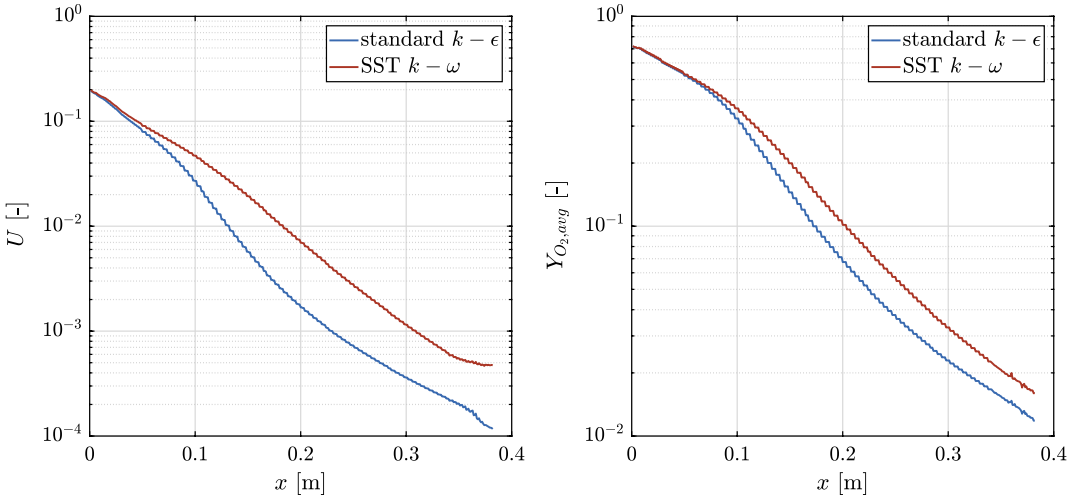

Fig. 9 Unmixedness (left) and average O_2 mass fraction (right) along the axial position.

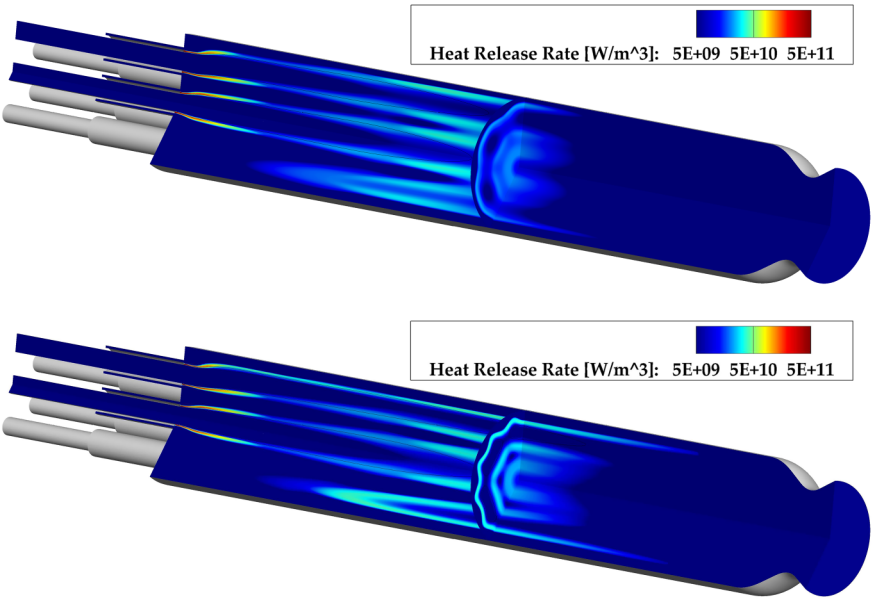

Fig. 10 Heat release field in the thrust chamber using the standard $k-\epsilon$ model (top) and the $k-\omega$ SST model (bottom). Axial scaling 50%.

held at a minimum. Chemical equilibrium calculations using the minimization of Gibb's free enthalpy showed that a mass fraction of approximately 0.2–0.4% O_2 is expected at equilibrium (depending on the pressure at the outlet plane). The O_2 mass fraction profiles along x are shown in Fig. 9. Both turbulence models seem to overpredict the oxygen at the outlet, thereby underpredicting the mixing and the energy release in the chamber. The $k-\epsilon$ and SST models show that approximately 1.40 and 1.75% O_2 remain unburnt, respectively. Therefore, although the $k-\epsilon$ produces better results than the SST, it still fails to capture the mixing and energy release correctly when combined with the flamelet model.

Finally, the fields of some major species are plotted in Fig. 12. Since the balance between CO and CO_2 is very important in methane/oxygen combustion and also affects the wall heat transfer characteristics, those species are chosen. It is observed that CO_2 is mainly generated in the areas around stoichiometry, as it is one of the two stoichiometric combustion products along with H_2O. CO, on the other hand, is mainly produced in regions with an absence of sufficient oxygen to generate CO_2. Since the common coaxial injector includes the fuel being injected in the outer annulus, the region close to the wall is fuel rich and facilitates the production of CO. As the mixing progresses, sufficient oxygen-rich gas reaches the wall and allows for the CO to react further and get converted to CO_2.

This effect is quantitatively shown in Fig. 13, in which the CO and CO_2 concentrations at the wall are presented as a function of the axial direction. For the simulation with SST, due to the poorer mixing, the production of CO at the wall is delayed. As a result, the point of maximal CO concentration is closer to the end of the chamber. This is also affecting the production of CO_2 at the wall; as the mixing is delayed, the gas at the wall starts getting leaner (closer to the global mixture fraction) at positions farther downstream, and then the transition of CO to CO_2 takes place. Furthermore, the SST model seems to predict a peak with higher concentrations of both CO and CO_2 at around $x = 0.02$ m from the face plate. This corresponds to the position of the stagnation point resulting from the recirculation zone (a shown in Sec. VI). This effect is less prominent in the simulation using the $k-\epsilon$. This higher concentration of reactants implies a stronger vortex formation and higher heat transfer at the stagnation point in the SST. This is verified in Fig. 11, in which the heat flux at the stagnation point is higher in the SST case.

Using an adiabatic flamelet model implies that no additional changes in the composition due to enthalpy defects are taken into account. Specifically, if a physically more intuitive nonadiabatic formulation were to be applied, the balance of CO and CO_2 at the wall would be different. As previous studies of methane/oxygen combustors have demonstrated, the low-enthalpy environment

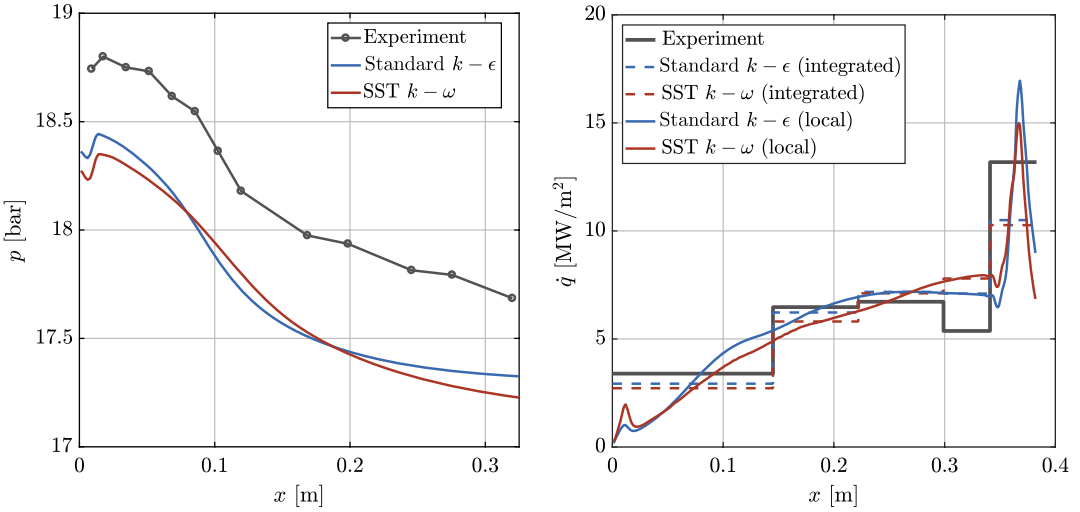

Fig. 11 Average pressure (left) and average wall heat flux (right) along the axial position.

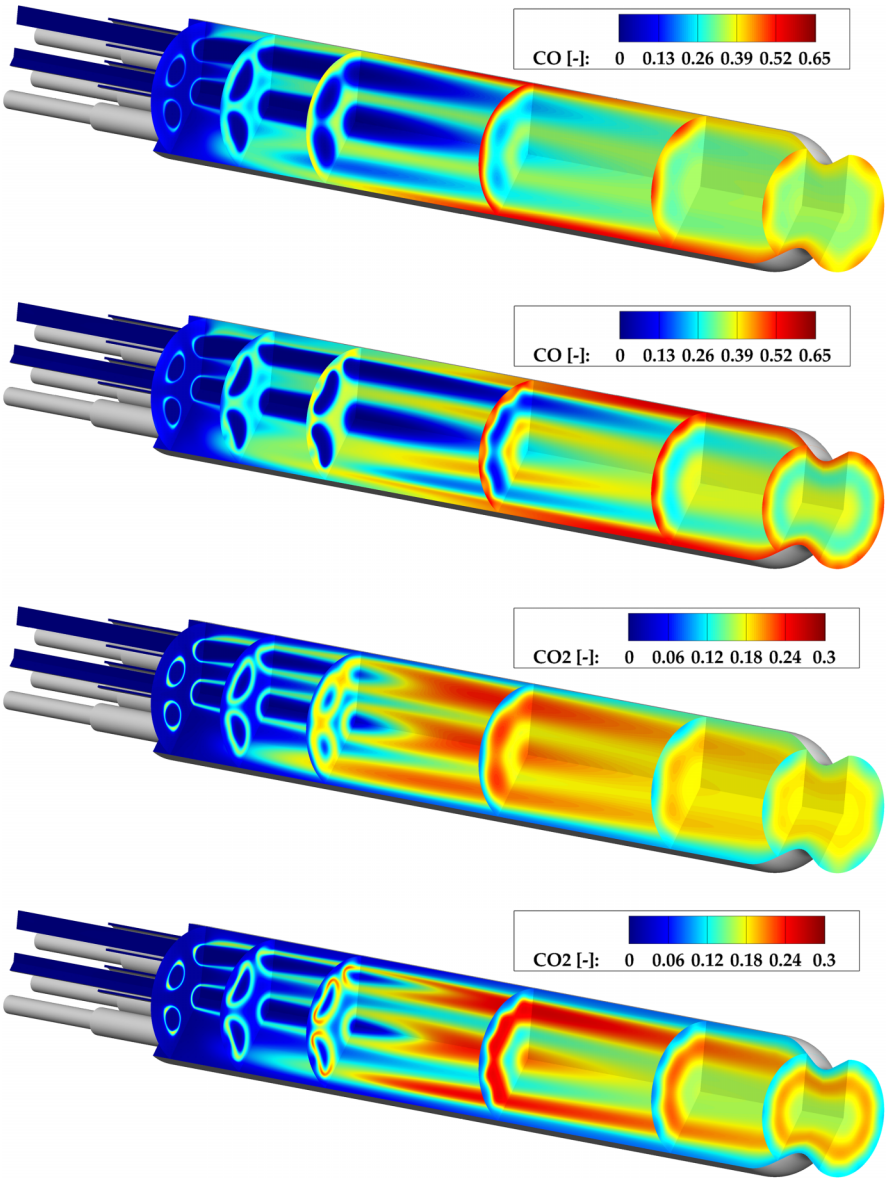

Fig. 12 CO and CO_2 fields in the thrust chamber using the standard $k-\epsilon$ model (top) and the $k-\omega$ SST model (bottom). Axial scaling 50%.

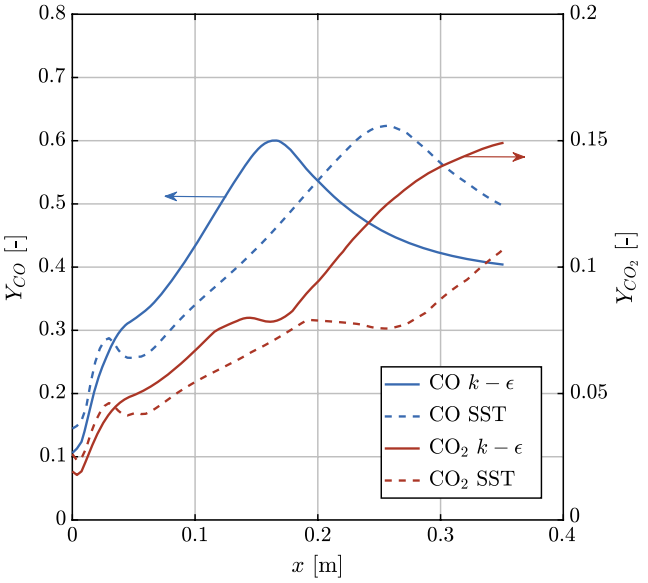

Fig. 13 CO and CO_2 concentrations at the chamber wall.

facilitates the recombination of CO to CO_2 [39]. This results in a faster depletion of CO compared to the frozen flamelet model in the vicinity of the wall and an increase in the heat transfer coefficient due to the exothermic nature of the recombination reaction.

B. Comparison with Experimental Results

The experimental pressure profile is displayed in Fig. 11. The profile shows a slight increase in the first axial positions, which corresponds to the presence of a stagnation point stemming from the injector recirculation zone, whereas after this point, a drop in the pressure values is observed. Both the increase at the stagnation point and the pressure drop are captured by the simulations. Comparing the absolute level gives as an additional indicator for the incompleteness of the combustion. Specifically, both turbulence models underestimate the pressure in the chamber by approximately 0.4 bar. The shape of the pressure profile seems to be very similar with the experimental one, implying similar acceleration profiles for the hot gas in the simulation and the experiment, but the absolute level is lower by around 2.5%. In the presence of recombination reactions due to the $k-\omega$ SST, the pressure profile seems to be slightly steeper close to the exit of the combustion chamber and the start of the nozzle, meaning that the energy release and the acceleration of the gas are still ongoing.

This is also the case with the heat flux, which keeps increasing even in the last chamber segment for the $k-\omega$ SST case, as can be seen in the right subfigure of Fig. 11, in which the local average heat flux (solid line) as well as the integrated heat flux for each segment (dashed line) are illustrated. Both the pressure and the heat flux profiles from the experiment demonstrate better agreement with the $k-\epsilon$ results. This fact combined with the unmixedness and O_2 profiles shown in Fig. 9 imply the ability of the $k-\epsilon$ to capture the mixing process more effectively.

Both models deliver a good match with the experimental data in the first three segments of the chamber. Similar slopes and average values are exhibited by both models. One difference is the heat flux directly at the stagnation point of the recirculation zone, which seems to be higher in the case for the SST $k-\omega$ model. This result agrees with the species profiles of Fig. 13. Apart from the stagnation point, the $k-\epsilon$ results show an increase of the heat flux over the first two segments and a flatter profile for the last two, indicating that the heat release has ended. In segment D, however, a drop in the heat flux was measured in the experiments, whereas the simulation predicted either a flat profile ($k-\epsilon$) or an increase of the heat loss to the wall ($k-\omega$ SST). This and the very high heat flux measured in the nozzle (compared to the CFD) are the main discrepancies between simulation and experiment. In fact, the nozzle heat flux has an error of approximately 25%. Further CFD tests were carried out by decreasing the wall temperature boundary condition since the actual value of the temperature is unknown. Even values of 300 K at the wall and simulations using a chemical equilibrium model were still unable to capture such a high increase in the nozzle heat flux. Changing the turbulence closure numbers for heat and mass transfer (Pr_t and Sc_t) did not introduce any improvement in this aspect.

A further investigation of the results and discussion with the publishers of the experimental results attributed the discrepancies in segments D and N to the experimental setup. Specifically, the nozzle had a separate cooling cycle, and for this test case, a very large water mass flow rate was chosen, in order to avoid any mechanical damage of the copper. The overly large coolant flow led to lower temperatures in the material and therefore to an axial heat flow from segment D into the nozzle segment. Energy that was originally applied to the wall of the fourth segment diffused axially toward the lower temperature domain of the nozzle segment. The consequence was that the water in the nozzle picked up a higher energy, whereas the water in the last segment was not heated as much as expected, thereby producing a significant drop in the heat flux of the third segment and a high increase in the nozzle.

V. Conjugate Heat Transfer

The effect of the cooling in the nozzle was also shown by Silvestri et al. [14] using an in-house engineering thermal code called Thermtest [40]. Thermtest allows the simulation of steady as well as transient thermal behavior of cooled or uncooled structures over a wide scope of chamber materials and cooling fluids. This demonstrated that the heat flux applied directly at the wall deviates from the one measured in the water manifolds, even in steady-state conditions. This effect is prominent only in the last two segments (D and N).

The basic assumption of the calorimetric measurement is that the integrated wall heat flux is identical to the water heat pickup. Hence, measuring the enthalpy difference of the incoming and outgoing water reproduces the average wall heat flux. In the present configuration, however, the assumption appears to be violated following the findings by Silvestri et al. [14]. Therefore, no wall heat flux data are available for segments D and N, and no comparison with the CFD results can be carried out.

To compare the CFD results with the available calorimetric data, an additional step has to be performed, in order to transform the obtained wall heat flux into a water enthalpy increase. To achieve that, a conjugate heat transfer (CHT) simulation of the copper structure and the cooling channels is carried out. Specifically, a 60 deg domain of the structure and coolant is modeled, and the commercial code ANSYS CFX is used for the numerical simulation of the coolant flow and heat conduction in the solid copper part of the thrust chamber. The first segment of the combustion chamber and the nozzle segment have rectangular cooling channels, whereas segments B, C, and D have circular channels, as shown by Silvestri et al. [12] and illustrated in Fig. 2. The 60 deg domain results in the incorporation of six rectangular cooling channels and five circular cooling channels, and corresponds to the smallest symmetrical domain. For the simulation, a block-structured grid with 27.8 million cells is used with the goal of fully resolving the boundary layer ($y^+ < 1$) at the cooling channel walls on the fluid domain side. The mesh of the cooling channels at the interface between segment D and segment N is shown in Fig. 14. Note that the mesh of the solid part is not shown in the figure but is included in the computational domain.

The boundary conditions for the cooling water with constant properties are defined according to the experiments, using a mass flow inlet condition together with a static pressure outlet condition. Because of numerical instabilities, the inflow of the combustion chamber cooling cycle is, however, approached by a total pressure boundary condition, which is dynamically adapted to keep the experimental target mass flow rate constant. Turbulence modeling is done by using Menter's $k-\omega$ SST model [20], neglecting any surface roughness effects. The heat conductivity of copper is modeled as a function of temperature. Between the combustion

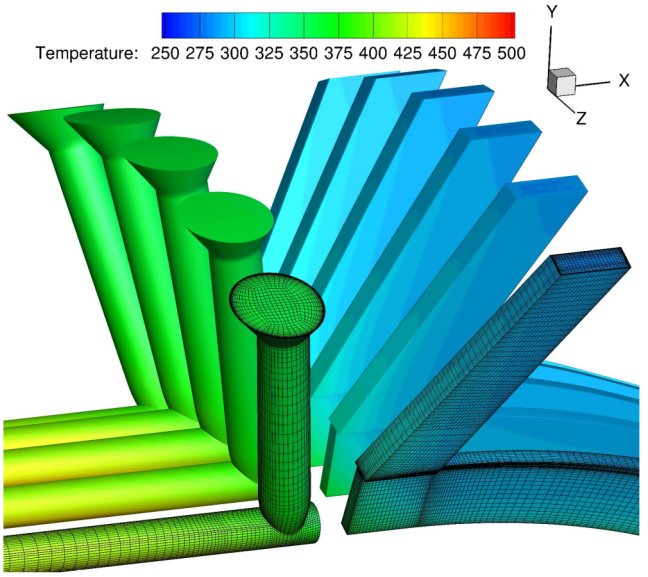

Fig. 14 Mesh of the cooling channels at the interface between segments D and N.

chamber segments, perfect heat transfer is assumed, while an adiabatic wall is set on the outer surfaces. For the simulation of the coolant flow, the equations for continuity, momentum, and energy are solved along with the transport equations for the turbulence kinetic energy and the specific dissipation rate, as shown in Sec. III. The setup is shown in detail in the work by Rahn et al. [41].

The study is carried out in two steps. In the first step, a one-way coupling is performed. The heat flux results obtained with a the one-dimensional wall temperature profile (Fig. 6) described in the previous section are fed to the model of the structure and coolant as von Neumann boundary conditions, and the resulting flow and heat transfer problem is solved. A single iteration of this coupling is carried out. In the second step, a fully coupled conjugate heat transfer simulation between the hot gas, structure, and coolant is performed. This implies a periodic exchange of the boundary conditions at the thrust chamber wall. Specifically, the heat flux obtained by the CFD of the hot gas is applied as a boundary condition at the structure wall and upon the solution of the structure and water simulation, the resulting wall temperature is applied as a boundary condition of the hot gas CFD. This process is iterated until convergence of the wall temperature and heat flux. Carrying out the fully coupled CHT is done to assess the validity of the one-way coupled results.

In the following subsections, the results using the heat flux from the hot gas simulation with the $k-\epsilon$ model as a boundary condition for the structure and cooling will be shown. The coupling with the SST hot gas simulation was also carried out but will be not used for the phenomenological description of the nozzle heat flux, as the previous sections demonstrated that the $k-\epsilon$ results are more reliable. The better agreement of the $k-\epsilon$ coupling with the experimental heat flux data will be demonstrated, however, once more in Fig. 15.

A. One-Way Coupling

The numerical results for the coolant and structural side resulting from the one-way conjugate heat transfer simulation are shown in Fig. 16 by using the temperature distribution. For the first cooling cycle covering the cylindrical combustion chamber part, a continuous increase in the fluid temperature through the channels together with a respective increase of the structural temperature is observed. This trend is locally interrupted by regions of colder temperatures near the hot gas wall in the vicinity of the cooling channels feeding lines.

The 3D effects of the wall temperature profile are shown in Fig. 17. As a result of the conjugate heat transfer simulation, an additional circumferential variation appears with higher temperatures occurring at a position of 0 deg above the injection element of the outer row. This highlights the importance of a 3D computation allowing one to resolve local peaks in the numerical simulation in order to evaluate the structural integrity. In contrast, the assumed boundary condition for the noncoupled hot gas simulation (black line) shows much lower temperatures with relative local deviations of the respective curves greater than 70 K in the combustion chamber. A similar relationship is observed when comparing the temperature values in the copper structure, which are evaluated at the exact positions of the thermocouple sensors used in the experimental setup. While very good agreement between the calculated and measured values is achieved in the chamber segment A, the simulation shows higher structural temperatures for the segments farther downstream. Similar behavior was reported in previous works carried out by Daimon et al. [42].

Possible sources causing this difference could also be found on the experimental side in the form of measurement errors, thermocouple positioning errors, or a deviation of the actual geometry from the CAD used as modeling input. Errors that could be introduced on the numerical side could be geometric simplifications in the form of omitting drilling tips together with adapting the diameter transition from the feeding channels to the main channel. Furthermore, not including any surface roughness effects could have an impact.

Both Figs. 16 and 17 also reveal a relatively low temperature of the throat and nozzle segment. This occurs due to the high experimental

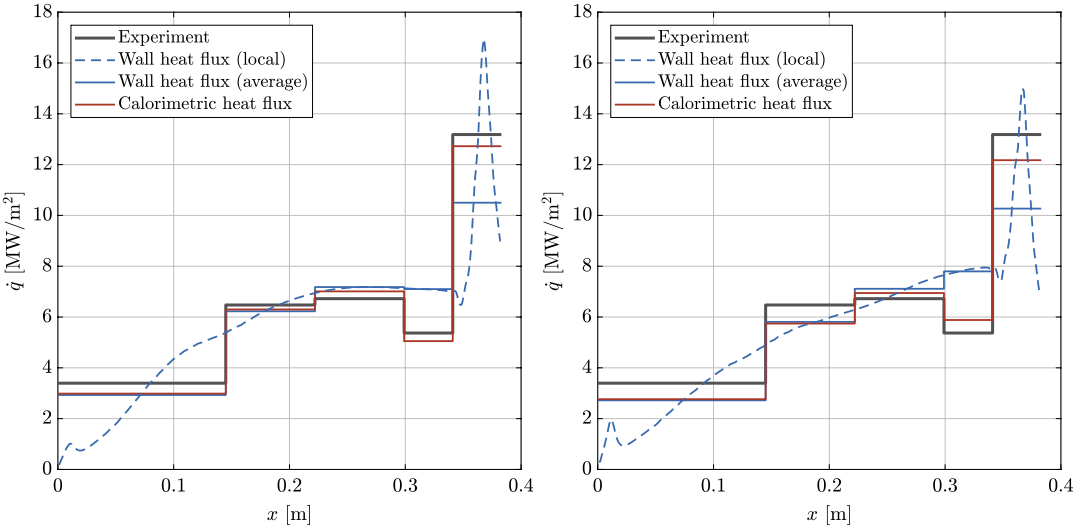

Fig. 15 Local and average wall heat flux compared to the experimental values and the calorimetric heat flux from the one-way coupling. Results with heat flux from hot gas simulation with $k-\epsilon$ (left) and SST (right).

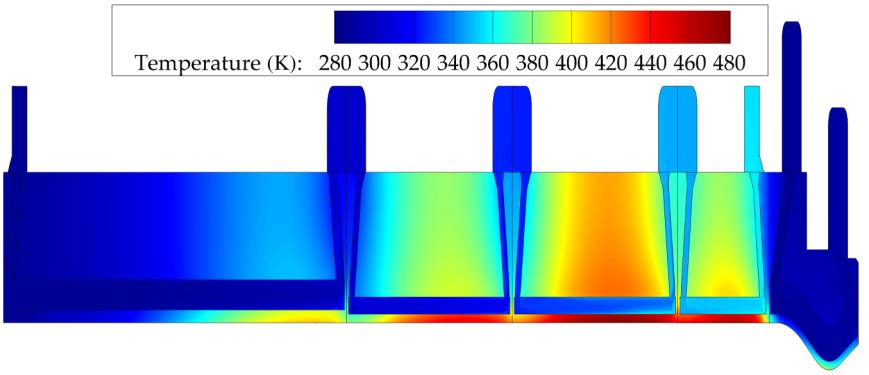

Fig. 16 Coolant side temperature field (axial scaling 25%) at the 0 deg plane (segments B, C, and D) and the 6 deg plane (segments A and N) to visualize all cooling channels above the outer injection element.

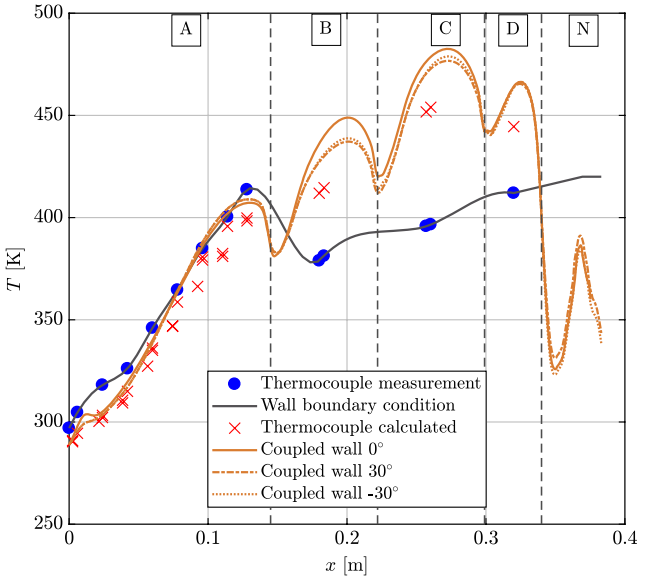

Fig. 17 Measured and calculated temperature values in the copper structure (points) and wall temperature boundary condition data (lines).

water mass flow rate in the nozzle cooling cycle, amounting to 5.5 times higher than the one in the cylindrical part. Moreover, the fact that both cycles are run in coflow operation results in hot water at the outlet of segment D being close to the fresh water flowing into the cooling channel of segment N. The resulting thermal gradient between segments D and N triggers axial heat conduction through the unisolated copper interface. Therefore, the nozzle cooling cycle extracts additional heat from the end of the chamber cooling cycle. Hence, the combustion chamber wall along the throat and nozzle segment has a much lower temperature compared to most of the cylindrical part, which has an additional impact on the wall heat flux prediction for the nozzle cooling cycle.

These effects have a large influence on the calorimetric wall heat flux prediction, as the data in Fig. 15 show. The calorimetric heat flux resulting from the one-way coupling of the hot gas and cooling channel simulations was evaluated as in the experiment, namely, according to Eq. (20).

$$\dot{q} = \dot{m}_w \frac{h_{\text{out}} - h_{\text{in}}}{A_w} \tag{20}$$

using the volume-averaged enthalpy difference between each manifold, the cooling cycle mass flow $\dot{m}_w$, and the combustion chamber wall surface area A_w. Both the results for $k-\epsilon$ (left) as well as SST (right) are shown. When comparing this calorimetric heat pickup (red line) to the experimental data (black line), better agreement between simulation and measurement is achieved. Compared to the heat flux directly at the wall (blue line), the calorimetric heat pickup shows a large deviation in the last two segments (D and N). As explained before, the effects discussed with regard to the throat and nozzle segment lower the heat pickup in segment D, while leading to a respective increase for segment N. In the remaining segments, however (A, B, and C), the differences between the wall heat flux and the calorimetric one are minimal.

This analysis shows that the experimental assumption of the wall heat flux and the calorimetric heat flux (resulting from the water enthalpy difference) being identical is not valid when large thermal gradients are present. With the one-sided coupling, the assumption of the axial heat flux altering the experimental data was confirmed, and a direct comparison between the nozzle results from CFD and from the experiment was carried out.

The relative deviation of the numerical calorimetric values from the experimental one shown in Table 4 defined as

$$\Delta\dot{q}_i = \frac{\dot{q}_{\text{exp}} - \dot{q}_i}{\dot{q}_{\text{exp}}} \tag{21}$$

provides a direct comparison between the performance of the standard $k-\epsilon$ and SST $k-\omega$. As expected, based on the results of Sec. IV, the less effective mixing of the SST model, which pushes the zone of heat release farther downstream, leads to a larger discrepancy in the heat flux values. Still, the error even with the SST model remains below 12% for most of the segments, with the exception of segment A. The larger deviation in segment A, which holds true also for the $k-\epsilon$ results, can be attributed to the fact that the heat flux in this region is highly dependent on the resolution of the recirculation zone. Since both the $k-\epsilon$ and the SST $k-\omega$ are eddy viscosity models and the recirculation zone is a region of anisotropic turbulence, they are not able to capture the turbulent heat flux accurately. However, for the remaining positions, the $k-\epsilon$ results manage to approximate the experimental values to an accuracy better than 6%. Therefore, the one-way coupling shows that the CFD heat flux results using the flamelet and $k-\epsilon$ models are able to match the experimental measurement with good agreement.

B. Two-Way Coupling

The two-way coupling is carried out by periodically exchanging the boundary conditions between the hot gas simulation and the structure/cooling channel simulation until the change between two subsequent iterations is smaller than a predefined threshold. Specifically, the simulation terminates when the maximal heat flux change between two iterations falls beneath 0.2%. For the hot gas

Table 4 Comparison of experimental and numerical calorimetric heat flux values

Model	$\Delta\dot{q}_A$, %	$\Delta\dot{q}_B$, %	$\Delta\dot{q}_C$, %	$\Delta\dot{q}_D$, %	$\Delta\dot{q}_N$, %
Standard $k-\epsilon$	12.07	2.71	−4.27	5.93	3.48
SST $k-\omega$	18.56	11.30	−3.30	−9.54	7.66

simulations, the Haswell nodes of the SuperMUC at the Leibniz Supercomputing Centre were used. The first iteration required approximately 25,000 CPU hours, whereas the subsequent iterations required approximately 1000 CPU hours each on 140 cores. The coolant simulation was performed using 15 CPUs (Intel Xeon CPU E5-2667 v3, 3.20 GHz) with 1000 CPU hours per iteration.

It was observed that the system achieved convergence after a small number of iterations (five iterations). This is an indicator for the fact that the initial solution provided (heat flux from the uncoupled hot gas simulation) is very close to the converged solution.

This is confirmed in Fig. 18. In the left subfigure, the uncoupled heat flux profile (shown already in Sec. IV) is compared to the converged solution of the coupled heat flux. In the right subfigure the relative difference between the two solutions is illustrated. The temperature difference in the same figure corresponds to the deviation of the converged wall temperature from the assumed initial wall boundary condition. It is observed in the right subfigure that the temperature applied as a boundary condition for the hot gas simulation in the converged CHT is up to 70 K higher than the initially applied thermal boundary condition in the chamber and up to 100 K lower in the nozzle. Despite this significant deviation, the two heat flux profiles are very similar, and their local discrepancies do not exceed 4% in any axial position. This implies that the wall temperature does not have a significant influence on the final heat flux profile as long as an adequately accurate first estimate is used, as was the case with the thermocouple measurements at 0.7 and 1.1 mm from the hot gas wall.

The reason for this low sensitivity is the fact that the wall heat transfer is driven by the difference in total enthalpy between the hot gas flow and the wall. For the present case with adiabatic temperatures of approximately 3500 K, the driving force is proportional to $T_{\mathrm{ad}} - T_w = 3500\ \mathrm{K} - 400\ \mathrm{K}$. The heat flux increase at the points of maximal deviation (assuming a temperature difference of 100 K) is hence expected to be in first order proportional to $(500-400)/(3500-400) \approx 3.2\%$, which is of the same order of magnitude as the observed values. Since the effect on the wall heat flux is minimal and since the correct wall temperature is almost never available a priori, the choice of an approximate temperature profile as a boundary condition of the hot gas CFD (e.g., like the one from Fig. 6) is justified.

The effect of the two-way coupling on the quantities of interest, namely, calorimetric heat flux and wall temperature, is given in Fig. 19. In the left subfigure, the calorimetric heat flux from the one-way coupling demonstrates only a minor deviation from the fully coupled simulation, which remains below 2%. For the nozzle segment, a slightly larger deviation is observed, which is expected, as this is the position with the highest wall temperature deviation as reported in Fig. 18.

Similarly, the temperature directly at the wall shows deviations that are constrained below 10 K. Therefore, one can safely deduce that the one-way coupling in this case is a sufficient approximation of a fully coupled simulation for the purpose of comparing with the experimental results, especially when considering the significantly lower computational cost.

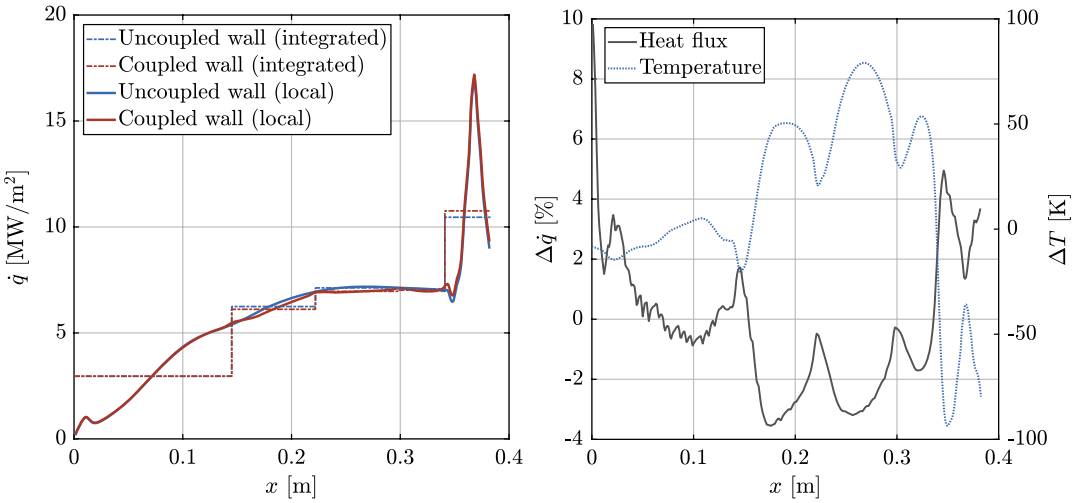

Fig. 18 Initial and converged wall heat flux (left). Wall temperature difference with corresponding relative heat flux change (right).

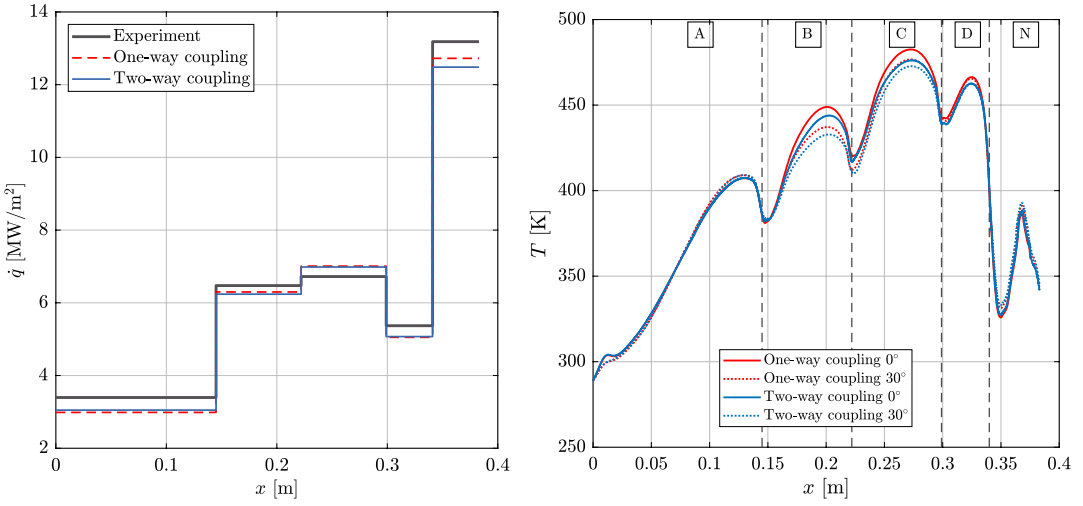

Fig. 19 Calorimetric heat flux (left) and wall temperature (right) from the one-way and two-way coupling.

VI. Azimuthal Heat Flux Profile

A very interesting observation occurs when investigating the variation of the heat flux along the chamber angle. The azimuthal profile of the heat flux at the wall is shown in Fig. 20. Here, 0 deg corresponds to the position directly above the injector, and −30, 30 deg corresponds to the symmetry planes, while 0 mm refers to the face plate, and 300 mm is a plane approximately 40 mm before the end of the combustion chamber and the beginning of the nozzle. As expected, the SST model produces a much larger variation of the heat flux value along the perimeter, since it has a higher temperature stratification even at positions close to the nozzle. The $k-\epsilon$ solution, on the other hand, demonstrates a flat heat flux profile for positions after 200 mm, in agreement with the temperature field (Fig. 7), which becomes homogeneous.

An unexpected effect is that for both models the heat flux has a local minimum at the position directly above the injector (0 deg) and its maximum at approximately 15 deg. This effect starts after about 50 mm downstream of the injector and continues for the rest of the chamber. To better understand the origin of this phenomenon, the temperature at the center of the first cell from the wall is plotted as seen in Fig. 21. At the wall position, the mixture fraction variance and the scalar dissipation tend to zero, and hence the temperature becomes a function of the mixture fraction solely (and the enthalpy, which, however, does not alter the chemical composition in the adiabatic flamelet formulation). For that reason, the mixture fraction is also plotted in Fig. 21. This is done only for the $k-\epsilon$ model, since it is the one producing the more physical results.

As expected, the temperature has a maximum directly at the positions where the heat flux is also maximal and a minimum at 0 deg. This is a result of the mixture fraction profiles at the wall; after the stoichiometric mixture fraction $Z_{st} = 0.2$, the temperature decreases with increasing mixture fraction, and hence the local maximum of the heat flux corresponds to a lower value of Z, i.e., a leaner composition, and vice versa. This is validated in the right subfigure of Fig. 21 and in Figs. 22 and 23. For positions closer to the injector, a recirculation zone is created, which leads to a maximum in temperature and heat flux right above the injector. Farther downstream, pockets of fuel-rich mixture are created directly at 0 deg, which leads to a decrease in temperature and heat flux. The shift in mixture fraction values above the injector is also visible in Fig. 22. Up until $x = 50$ mm, the mixture fraction at 0 deg is smaller than between the injectors, and downstream of that point, a shift occurs leading to colder, high- Z gas pockets being concentrated at 0 deg.

The streamlines in Figs. 24 and 25 verify that. In Fig. 24, the length of the recirculation zone is visible, amounting to approximately 10 mm, whereas in Fig. 25, the cause of the higher mixture fraction at 0 deg is illustrated. It can be observed that after the location of the recirculation zone a twist in the flow takes place. Specifically, due to the interaction of the injector jet with the symmetry boundary condition (i.e., with the neighboring injector), areas with a high mixture fraction are pushed toward the middle. This leads to an accumulation of the fuel-rich zones above the injector, leading to a lower temperature.

The presence of a strong vortex system feeding the hot, oxidizer-rich fuel toward the wall at the ±10–15 deg position is visible when examining the vorticity field in the chamber. Specifically, the vorticity component along the axial direction $\Omega_x = (\partial u_z/\partial y) - (\partial u_y/\partial z)$ is shown at selected planes in Fig. 26. Starting close to the face plate (at $x = 20$ mm), two locations with strong vorticity

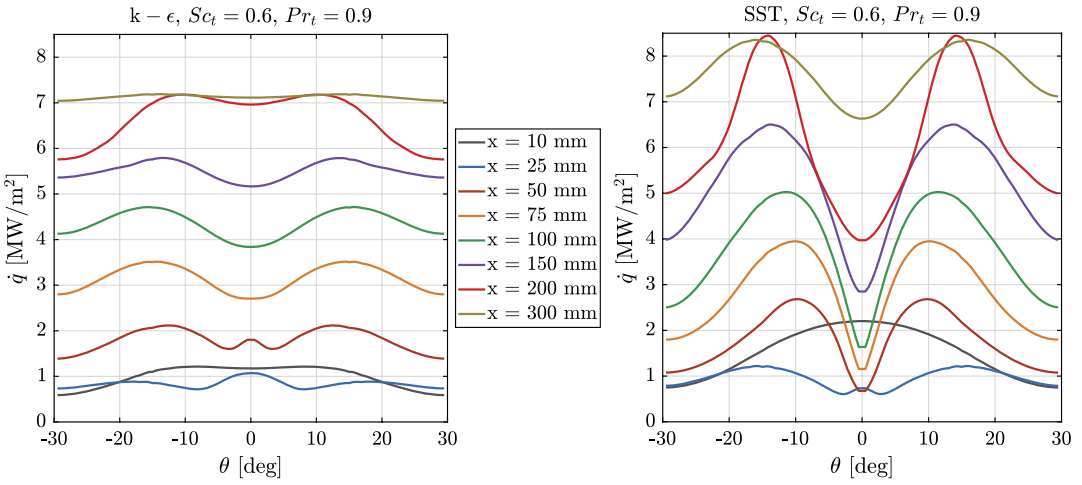

Fig. 20 Heat flux variation along the chamber angle for different axial positions.

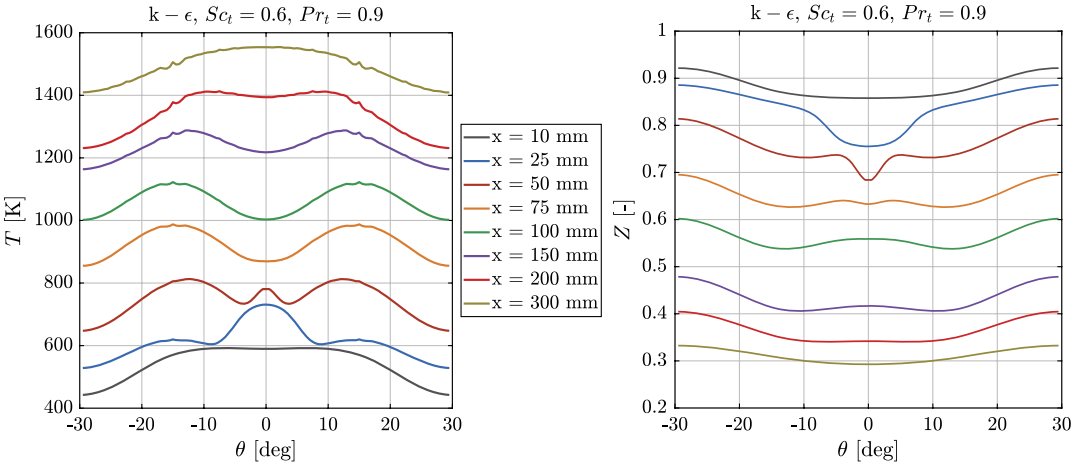

Fig. 21 Azimuthal variation of temperature and mixture fraction at the wall for the $k-\epsilon$ model.

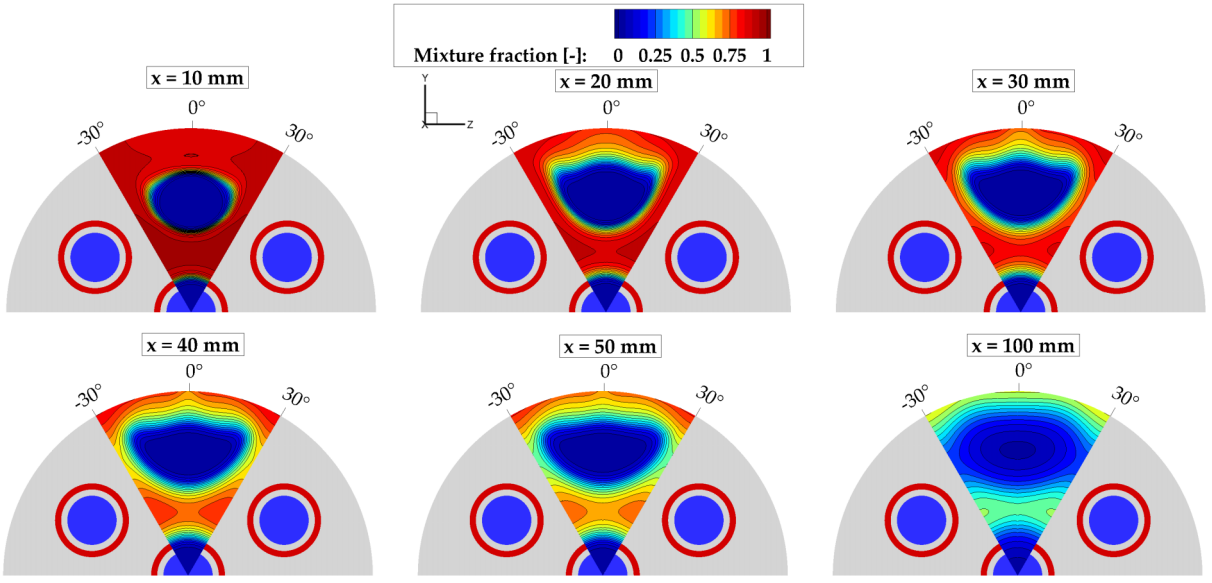

Fig. 22 Contour plot of mixture fraction at different planes in the thrust chamber.

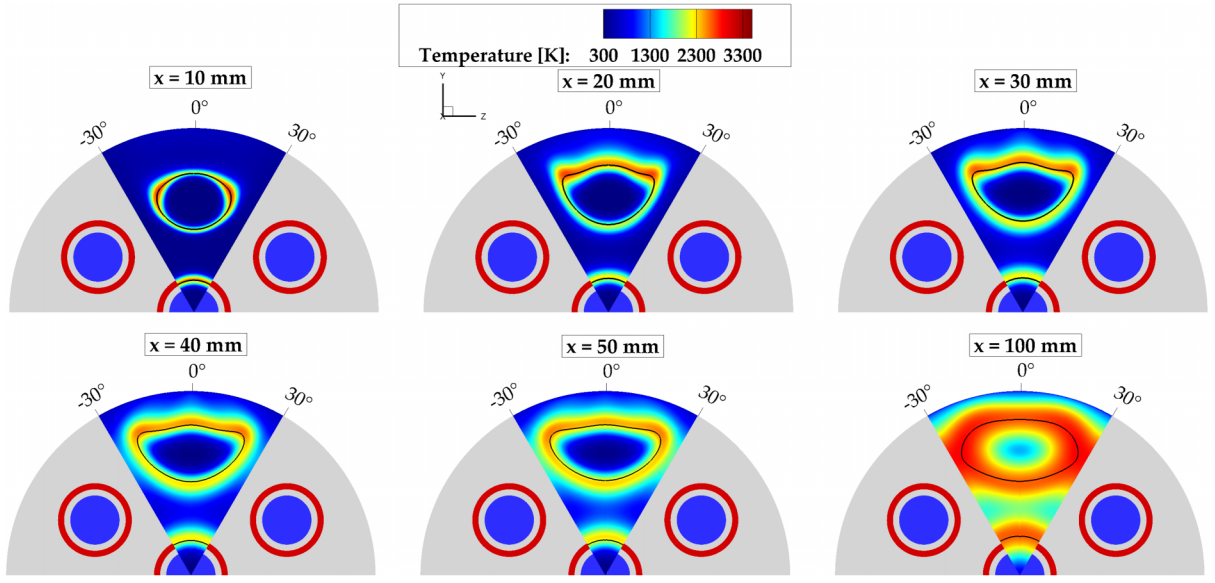

Fig. 23 Contour plot of temperature at different planes in the thrust chamber.

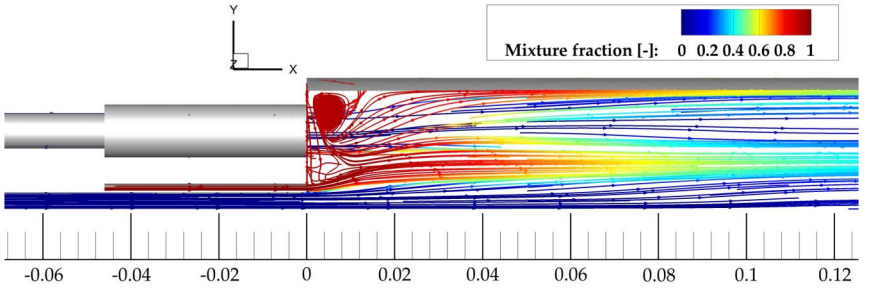

Fig. 24 Streamlines coloured by mixture fraction, showing the recirculation zone.

components appear at ±10–15 deg. This system of vortices appears to circulate hot gas from the shear layer of the coaxial injector directly onto the wall and serves as the main driving force for the increased heat transfer coefficient at this angular position. Moreover, this explains the shape of the temperature field in Fig. 23. In the first 10 mm from the face plate, the interaction between the individual flames is weak, and the expansion of the flame occurs nearly cylindrical, homogeneously in all radial directions. As soon as the jet/jet interaction is strengthened, the temperature field becomes distorted, and the expansion occurs preferably upward toward the wall. The vortex system, which is responsible for this distortion, is a consequence of the radial expansion of the individual jets and enhances the local heat loads between the injectors.

At positions farther downstream, the presence of the vortex system is still visible, but it appears to weaken after approximately 100 mm. At those positions, the individual jets are no longer dominant, and a

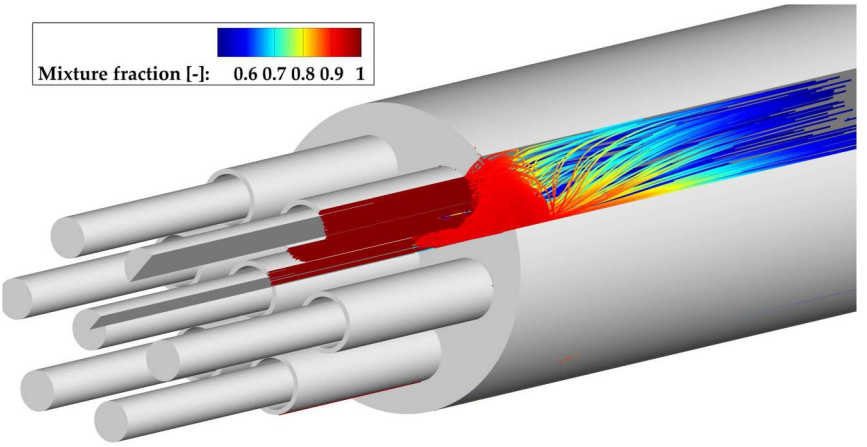

Fig. 25 Streamlines coming from the fuel inlet colored by the mixture fraction.

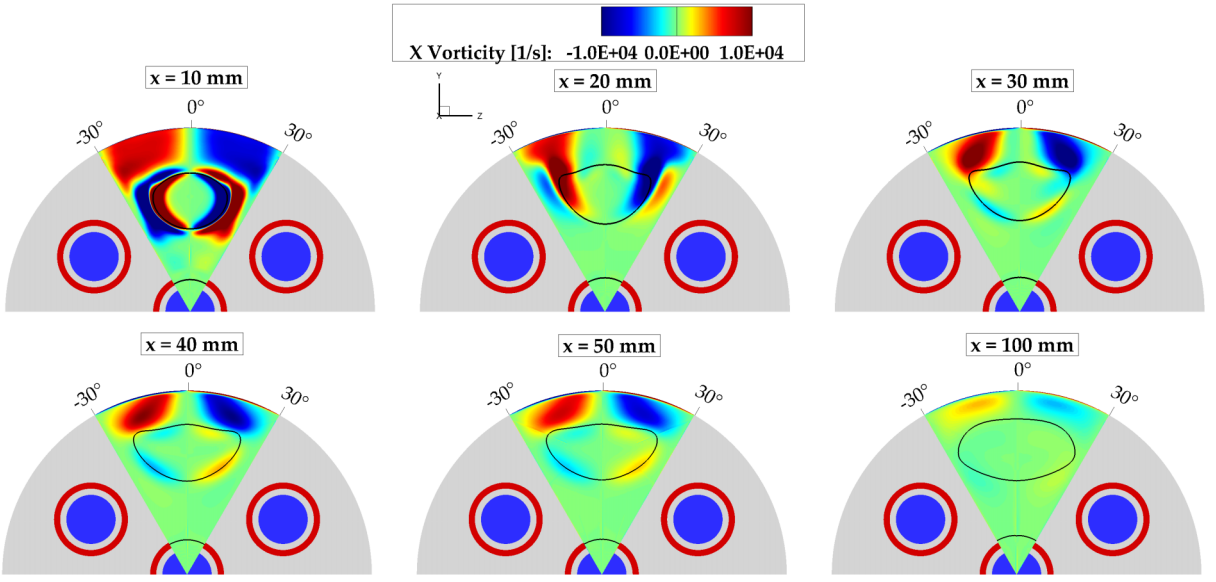

Fig. 26 Contour plot of vorticity at different planes in the thrust chamber.

homogeneous flow is achieved, which explains the absence of a strong recirculation zone. Because of the lack of a driving force for a circulation of hot gas toward the wall, at positions downstream of 100 mm, the temperature and heat flux distribution appears to smoothen, leading to a flatter profile.

To make sure that the effect is not caused by the symmetry boundary condition applied between the injectors, it was decided to extend the computational domain to include 120 deg of the rocket combustor. This has the effect of modeling two full injectors at the outer row (instead of half) as well as one direct interaction between the injectors and one through the symmetry boundary condition. To keep the computational mesh intact, the original mesh was simply reflected onto the symmetry plane to maintain the same resolution.

The results demonstrated an identical heat flux profile as the 30 deg calculation, indicating that the symmetry boundary condition is not the source of the local minimum. This is shown in Fig. 27, in which the azimuthal heat flux distribution for five different axial positions is illustrated. The 0 and 60 deg positions correspond to the two injector elements, whereas the −30, 30, and 90 deg positions correspond to the planes between injectors. The solid lines in Fig. 27 represent the solution using the 120 deg domain, whereas the symbols represent the 30 deg solution. By examining the plots, it is evident that the 30 deg symmetry is capable of resolving the azimuthal profiles with deviations smaller than 1% from the 120 deg one.

This effect is therefore a result of the turbulence model, the chemistry model, and the flow interaction between the injectors.

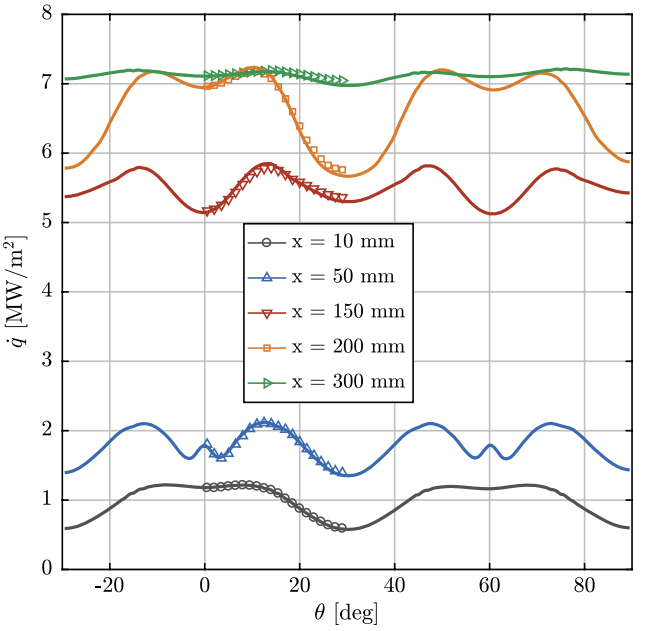

Fig. 27 Azimuthal heat flux profiles for 120 deg and 30 deg domains.

Further studies with other combustion models should be carried out to examine if this is only produced due to the use of the flamelet approach. Further measurement data such as an azimuthal heat flux profile would also be beneficial in order to allow a comparison with the CFD.

VII. Conclusions

A 3D Reynolds-averaged Navier–Stokes simulation of a seven-element rocket thrust chamber operated with GOX/GCH_4 was carried out. For the simulation, an adiabatic flamelet approach was implemented using a skeletal chemical mechanism. To allow for a comparison with experimental calorimetric heat fluxes, one-way and two-way couplings with the simulation of the structure and cooling channels were carried out.

Two different turbulence models were compared to each other, and specifically the $k-\epsilon$ with a two-layer model was compared to the $k-\omega$ shear-stress transport (SST). It was found that the $k-\epsilon$ produced more physical results in the combustion chamber, since it facilitated mixing, whereas the SST produced a very large temperature stratification, which propagated farther downstream until the nozzle. This was attributed to a much lower turbulent viscosity in the main flow. However, even the $k-\epsilon$ was found to have inefficient mixing and a lower heat release than theoretically expected. This was evident due to a high unmixedness at the exit, a high mass fraction of unburnt oxygen, and a chamber pressure lower than the experimental one by 2.5%. A further reason for the low pressure is that the adiabatic model fails to capture recombination reactions occurring at lower enthalpy levels. The heat release of those exothermic reactions that is not present in the frozen flamelet chemistry could be the culprit for the lower pressure, and nonadiabatic extensions of the model are needed to capture the effect.

Apart from the pressure, comparison with the experimental heat flux took place. The computational fluid dynamics (CFD) simulation was able to reproduce the heat flux values in the first three segments of the combustion chamber but produced a high discrepancy in the last segment and in the nozzle. To understand the nature of this deviation, a one-way coupling with the simulation of the thrust chamber structure and coolant flow was carried out using the wall heat flux from CFD as a boundary condition. This analysis showed a significant deviation between the calorimetrically measured heat flux from the one applied directly onto the hot gas wall. The source of this disagreement was found to be due to the experimental setup. An overestimated coolant mass flow rate in the nozzle produced very large thermal gradients in the structure, resulting in an unrealistically high measured heat flux in the nozzle. After taking into account this effect, very good agreement between simulation and experiment was found.

To evaluate the validity of the one-way coupling, a two-way coupling was also carried out by periodically exchanging the boundary conditions of the hot gas simulation and the cooling channel simulation until convergence. It was found that no significant change compared to the one-way coupling was present. This is attributed to the low sensitivity of the hot gas heat flux on the wall temperature boundary condition. Differences of up to 100 K in the wall temperature resulted in changes of approximately 4% in the heat flux. Therefore, carrying out simulations with approximate temperature profiles for the temperature (since wall temperature is rarely known a priori) is considered to be justified.

Finally, it was observed that the heat flux coming from the CFD had a local minimum directly above the injector position (0 deg) as opposed to a maximum. This was attributed to the interaction between the individual jets leading to low-temperature gas staying trapped directly above the injector position. A further simulation with a 120 deg domain confirmed that this effect was not a product of the symmetry boundary conditions.

Further examination of this test case is planned for the future. For an improved modeling of the heat transfer with the wall, a nonadiabatic flamelet model will be applied, which will include heat loss effects in the concentration of the species via recombination. Further evaluation of the test results is also scheduled; by developing an inverse heat transfer method, the azimuthal distribution of the heat flux could be reconstructed based on the temperature measurements at the wall. This would allow for a verification or disproving of the heat flux profile along the chamber perimeter. Simulations with large-eddy simulation will also be carried out to see if the behavior of the jet interaction remains.

Acknowledgments

Financial support has been provided by the German Research Foundation in the framework of the Sonderforschungsbereich Transregio 40: "Technological Foundation for the Thermally and Mechanically High Loaded Components of Future Space Transportation System". The authors gratefully acknowledge the Gauss Centre for Supercomputing e.V. (www.gauss-centre.eu) for funding this project by providing computing time on the Gauss Center for Supercomputing supercomputer SuperMUC at Leibniz Supercomputing Centre (www.lrz.de). The additional work on the coolant flow simulations at ArianeGroup has been supported by the Bayerische Forschungsstiftung within the project "Umweltfreundliche Treibstoffkombination LOX/Methan" and by the national technology program TARES 2020 sponsored by the DLR, German Aerospace Center, Bonn, Germany, under contract number 50RL1710.

References

[1] Frey, M., Aichner, T., Görgen, J., Ivancic, B., Kniesner, B., and Knab, O., "Modeling of Rocket Combustion Devices," *10th AIAA/ASME Joint Thermophysics and Heat Transfer Conference*, AIAA Paper 2009-5477, 2010. doi:10.2514/6.2009-5477

[2] Urbano, A., Selle, L., Staffelbach, G., Cuenot, B., Schmitt, T., Ducruix, S., and Candel, S., "Exploration of Combustion Instability Triggering Using Large Eddy Simulation of a Multiple Injector Liquid Rocket Engine," *Combustion and Flame*, Vol. 169, July 2016, pp. 129–140. doi:10.1016/j.combustflame.2016.03.020

[3] Oefelein, J. C., and Yang, V., "Modeling High-Pressure Mixing and Combustion Processes in Liquid Rocket Engines," *Journal of Propulsion and Power*, Vol. 14, No. 5, 1998, pp. 843–857. doi:10.2514/2.5349

[4] Zhukov, V. P., "Computational Fluid Dynamics Simulations of a GO2/GH2 Single Element Combustor," *Journal of Propulsion and Power*, Vol. 31, No. 6, 2015, pp. 1707–1714. doi:10.2514/1.B35654

[5] Cutrone, L., De Palma, P., Pascazio, G., and Napolitano, M., "A RANS Flamelet-Progress-Variable Method for Computing Reacting Flows of Real-Gas Mixtures," *Computers & Fluids*, Vol. 39, No. 3, 2010, pp. 485–498. doi:10.1016/j.compfluid.2009.10.001

[6] Zips, J., Müller, H., and Pfitzner, M., "Efficient Thermo-Chemistry Tabulation for Non-Premixed Combustion at High-Pressure Conditions," *Flow, Turbulence and Combustion*, Vol. 101, No. 3, 2018, pp. 821–850. doi:10.1007/s10494-018-9932-4

[7] Negishi, H., Daimon, Y., and Kawashima, H., "Flowfield and Heat Transfer Characteristics in the LE-X Expander Bleed Cycle Combustion Chamber," *50th AIAA/ASME/SAE/ASEE Joint Propulsion Conference*, AIAA Paper 2014-4010, 2014. doi:10.2514/6.2014-4010

[8] Negishi, H., Kumakawa, A., Yamanishi, N., and Kurosu, A., "Heat Transfer Simulations in Liquid Rocket Engine Subscale Thrust Chambers," *44th AIAA/ASME/SAE/ASEE Joint Propulsion Conference & Exhibit*, AIAA Paper 2008-5241, 2008. doi:10.2514/6.2008-5241

[9] Betti, B., Martelli, E., and Nasuti, F., "Heat Flux Evaluation in Oxygen/Methane Thrust Chambers by RANS Approach," *46th AIAA/ASME/SAE/ASEE Joint Propulsion Conference & Exhibit*, AIAA Paper 2010-6721, 2010. doi:10.2514/6.2010-6721

[10] Kim, S.-K., Joh, M., Choi, H. S., and Park, T. S., "Multidisciplinary Simulation of a Regeneratively Cooled Thrust Chamber of Liquid Rocket Engine: Turbulent Combustion and Nozzle Flow," *International Journal of Heat and Mass Transfer*, Vol. 70, March 2014, pp. 1066–1077. doi:10.1016/j.ijheatmasstransfer.2013.10.046

[11] Song, J., and Sun, B., "Coupled Numerical Simulation of Combustion and Regenerative Cooling in LOX/Methane Rocket Engines," *Applied Thermal Engineering*, Vol. 106, Aug. 2016, pp. 762–773. doi:10.1016/j.applthermaleng.2016.05.130

[12] Silvestri, S., Celano, M. P., Schlieben, G., and Haidn, O. J., "Characterization of a Multi-Injector GOX-GCH4 Combustion Chamber," *52nd AIAA/SAE/ASEE Joint Propulsion Conference*, AIAA Paper 2016-4992, 2016. doi:10.2514/6.2016-4992

[13] Chemnitz, A., Sattelmayer, T., Roth, C., Haidn, O., Daimon, Y., Keller, R., Gerlinger, P., Zips, J., and Pfitzner, M., "Numerical Investigation of Reacting Flow in a Methane Rocket Combustor: Turbulence Modeling," *Journal of Propulsion and Power*, Vol. 34, No. 4, 2018, pp. 864–877. doi:10.2514/1.B36565

[14] Silvestri, S., Kirchberger, C., Schlieben, G., Celano, M. P., and Haidn, O., "Experimental and Numerical Investigation of a Multi-Injector GOX-GCH4 Combustion Chamber," *Transactions of the Japan Society for Aeronautical and Space Sciences, Aerospace Technology Japan*, Vol. 16, No. 5, 2018, pp. 374–381. doi:10.2322/tastj.16.374

[15] Richardson, L. F., "The Approximate Arithmetical Solution by Finite Differences of Physical Problems Involving Differential Equations, with an Application to the Stresses in a Masonry Dam," *Philosophical Transactions of the Royal Society London, Series A: Mathematical and Physical Sciences*, Vol. 210, Nos. 459–470, 1911, pp. 307–357. doi:10.1098/rsta.1911.0009

[16] Kays, W. M., "Turbulent Prandtl Number-Where Are We?" *Journal of Heat Transfer*, Vol. 116, No. 2, 1994, pp. 284–295. doi:10.1115/1.2911398

[17] Riedmann, H., Kniesner, B., Frey, M., and Munz, C.-D., "Modeling of Combustion and Flow in a Single Element GH2/GO2 Combustor," *Council of European Aerospace Societies Space Journal*, Vol. 6, No. 1, 2014, pp. 47–59. doi:10.1007/s12567-013-0056-3

[18] Launder, B. E., and Spalding, D. B., *Mathematical Models of Turbulence*, Academic Press, London, 1972, pp. 137–152.

[19] Wolfshtein, M., "The Velocity and Temperature Distribution in One-Dimensional Flow with Turbulence Augmentation and Pressure Gradient," *International Journal of Heat and Mass Transfer*, Vol. 12, No. 3, 1969, pp. 301–318. doi:10.1016/0017-9310(69)90012-X

[20] Menter, F. R., "Two-Equation Eddy-Viscosity Turbulence Models for Engineering Applications," *AIAA Journal*, Vol. 32, No. 8, 1994, pp. 1598–1605. doi:10.2514/3.12149

[21] Wilcox, D. C., *Turbulence Modeling for CFD*, Vol. 2, DCW Industries, La Canada, CA, 1998, pp. 124–128.

[22] Jones, W., and Whitelaw, J., "Calculation Methods for Reacting Turbulent Flows: A Review," *Combustion and Flame*, Vol. 48, 1982, pp. 1–26. doi:10.1016/0010-2180(82)90112-2

[23] Peters, N., "Laminar Diffusion Flamelet Models in Non-Premixed Turbulent Combustion," *Progress in Energy and Combustion science*, Vol. 10, No. 3, 1984, pp. 319–339. doi:10.1016/0360-1285(84)90114-X

[24] Pitsch, H., Barths, H., and Peters, N., "Three-Dimensional Modeling of NOx and Soot Formation in DI-Diesel Engines Using Detailed Chemistry Based on the Interactive Flamelet Approach," Soc. of Automotive Engineers International Paper 962057, Warrendale, PA, 1996. doi:10.4271/962057

[25] Lee, D., Thakur, S., Wright, J., Ihme, M., and Shyy, W., "Characterization of Flow Field Structure and Species Composition in a Shear Coaxial Rocket GH2/GO2 Injector: Modeling of Wall Heat Losses," *47th AIAA/ASME/SAE/ASEE Joint Propulsion Conference & Exhibit*, AIAA Paper 2011-6125, 2011. doi:10.2514/6.2011-6125

[26] Rahn, D., Riedmann, H., Behr, R., and Haidn, O. J., "Non–Adiabatic Flamelet Modeling for the Numerical Simulation of Methane Combustion in Rocket Thrust Chambers," *54th AIAA/SAE/ASEE Joint Propulsion Conference*, AIAA Paper 2018-4869, 2018. doi:10.2514/6.2018-4869

[27] Perakis, N., Roth, C., and Haidn, O. J., "Development of a Non-Adiabatic Flamelet Model for Reacting Flows with Heat Loss," *Space Propulsion Conference*, Association Aéronautique et Astronautique de France Paper 171, 2018.

[28] Fiorina, B., Baron, R., Gicquel, O., Thevenin, D., Carpentier, S., and Darabiha, N., "Modelling Non-Adiabatic Partially Premixed Flames Using Flame-Prolongation of ILDM," *Combustion Theory and Modelling*, Vol. 7, No. 3, 2003, pp. 449–470. doi:10.1088/1364-7830/7/3/301

[29] Cecere, D., Giacomazzi, E., Picchia, F. R., Arcidiacono, N., Donato, F., and Verzicco, R., "A Non-Adiabatic Flamelet Progress–Variable Approach for LES of Turbulent Premixed Flames," *Flow, Turbulence and Combustion*, Vol. 86, No. 3, 2011, pp. 667–688. doi:10.1007/s10494-010-9319-7

[30] Marracino, B., and Lentini, D., "Radiation Modelling in Non-Luminous Nonpremixed Turbulent Flames," *Combustion Science and Technology*, Vol. 128, Nos. 1–6, 1997, pp. 23–48. doi:10.1080/00102209708935703

[31] Chan, S., Pan, X., and Abou-Ellail, M., "Flamelet Structure of Radiating CH4-Air Flames," *Combustion and Flame*, Vol. 102, No. 4, 1995, pp. 438–446. doi:10.1016/0010-2180(95)00037-7

[32] Proch, F., and Kempf, A., "Modeling Heat Loss Effects in the Large Eddy Simulation of a Model Gas Turbine Combustor with Premixed Flamelet Generated Manifolds," *Proceedings of the Combustion Institute*, Vol. 35, No. 3, 2015, pp. 3337–3345. doi:10.1016/j.proci.2014.07.036

[33] Kishimoto, A., Moriai, H., Takenaka, K., Nishiie, T., Adachi, M., Ogawara, A., and Kurose, R., "Application of a Nonadiabatic Flamelet/Progress-Variable Approach to Large-Eddy Simulation of H2/O2 Combustion Under a Pressurized Condition," *Journal of Heat Transfer*, Vol. 139, No. 12, 2017. doi:10.1115/1.4037099

[34] Ma, P. C., Wu, H., Ihme, M., and Hickey, J.-P., "Nonadiabatic Flamelet Formulation for Predicting Wall Heat Transfer in Rocket Engines," *AIAA Journal*, Vol. 56, No. 6, 2018, pp. 2336–2349. doi:10.2514/1.J056539

[35] Slavinskaya, N., Abbasi, M., Starcke, J.-H., Mirzayeva, A., and Haidn, O. J., "Skeletal Mechanism of the Methane Oxidation for Space Propulsion Applications," *52nd AIAA/SAE/ASEE Joint Propulsion Conference*, AIAA Paper 2016-4781, 2016. doi:10.2514/6.2016-4781

[36] Hirschfelder, J. O., Curtiss, C. F., Bird, R. B., and Mayer, M. G., *Molecular Theory of Gases and Liquids*, Wiley, New York, 1954, pp. 1167–1173.

[37] Bird, R. B., Stewart, W. E., and Lightfoot, E. N., *Transport Phenomena*, Wiley, New York, 1960, pp. 274–278.

[38] Wilke, C., "A Viscosity Equation for Gas Mixtures," *Journal of Chemical Physics*, Vol. 18, No. 4, 1950, pp. 517–519. doi:10.1063/1.1747673

[39] Perakis, N., Roth, C., and Haidn, O., "Simulation of a Single-Element Rocket Combustor Using a Non-Adiabatic Flamelet Model," *Space Propulsion Conference 2018*, Association Aéronautique et Astronautique de France Paper 174, 2018.

[40] Kirchberger, C., Wagner, R., Kau, H.-P., Soller, S., Martin, P., Bouchez, M., and Bonzom, C., "Prediction and Analysis of Heat Transfer in Small Rocket Chambers," *46th AIAA Aerospace Sciences meeting and Exhibit*, AIAA Paper 2008-1260, 2008, pp. 7–11. doi:10.2514/6.2008-1260

[41] Rahn, D., Eiringhaus, D., Riedmann, H., Behr, R., and Haidn, O. J., "Characterization of an Adiabatic Flamelet Combustion Model for Gaseous CH4/O2 Combustion in Rocket Thrust Chambers," *Space Propulsion Conference*, Association Aéronautique et Astronautique de France Paper 152, 2018.

[42] Daimon, Y., Negishi, H., Silvestri, S., and Haidn, O. J., "Conjugated Combustion and Heat Transfer Simulation for a 7 Element GOX/GCH4 Rocket Combustor," *2018 Joint Propulsion Conference*, AIAA Paper 2018-4553, 2018. doi:10.2514/6.2018-4553

V. Raman
Associate Editor